

**PONTIFICIA UNIVERSIDAD  
CATÓLICA DEL PERÚ**

**Escuela de Posgrado**



**Joint Reconstruction Techniques for Ultrasonic Attenuation  
Imaging**

Tesis para obtener el grado académico de Maestro en  
Procesamiento de Señales e Imágenes Digitales que presenta:

*Edmundo Arom Miranda Zárate*

**Asesor:**

*Roberto Janniel Lavarello Montero*

**Lima, 2024**


## Informe de Similitud

Yo, Roberto Janniel Lavarello Montero, docente de la Escuela de Posgrado de la Pontificia Universidad Católica del Perú, asesor de la tesis titulada Joint Reconstruction Techniques for Ultrasonic Attenuation Imaging, del autor Edmundo Arom Miranda Zárate, dejo constancia de lo siguiente:

- El mencionado documento tiene un índice de puntuación de similitud de 28%. Así lo consigna el reporte de similitud emitido por el software *Turnitin* el 4/04/2024. No obstante, se tienen que omitir las referencias 1 y 3 del informe, ya que corresponden a trabajos del mismo alumno. El índice de similitud, omitiendo las referencias señaladas, es de 16%, lo que está dentro del límite establecido.
- He revisado con detalle dicho reporte y la Tesis o Trabajo de investigación, y no se advierte indicios de plagio.
- Las citas a otros autores y sus respectivas referencias cumplen con las pautas académicas.

Lugar y fecha:

Lima, 5 de Abril de 2024.

Apellidos y nombres del asesor / de la asesora: Lavarello Montero, Roberto Janniel	
DNI: 10544227	Firma 
ORCID: 0000-0001-8472-5161	

## Resumen

El ultrasonido cuantitativo (QUS, por sus siglas en inglés) es una modalidad de imagen no invasiva que caracteriza numéricamente los tejidos para el diagnóstico médico. Los estimadores QUS se basan en parámetros acústicos como la pendiente del coeficiente de atenuación (ACS, por sus siglas en inglés). Un estudio anterior propuso eliminar el ruido de las relaciones logarítmicas espectrales utilizando una variación total de un solo canal a través de la frecuencia. El método espectral para estimar el ACS, conocido como diferencia logarítmica espectral (SLD, por sus siglas en inglés) no incorpora ninguna estrategia de reconstrucción conjunta para mejorar la imagen. Por lo tanto, este trabajo propone la integración de dos estrategias conjuntas compatibles con el marco SLD. Primero, un enfoque de regularización conjunta denominado variación total nuclear (TNV-SLD) es implementado, el cual combina información geométrica del ACS y el componente del coeficiente de retrodispersión (BSC, por sus siglas en inglés) para mejorar la calidad de las imágenes, logrando mejores resultados en términos de error porcentual medio (MPE) y relación contraste-ruido (CNR). Posteriormente, el estudio se amplía para eliminar conjuntamente los ratios logarítmicos espectrales del SLD en los canales de frecuencia. Se propone un método conjunto multifrecuencia para aumentar la calidad de las imágenes de atenuación. Se consideraron dos modificaciones de la variación total con base en las normas Frobenius (TFV) y nuclear (TNV). Las métricas se compararon con dos métodos de regularización anteriores denominados RSLD y TVSLD, basados en la variación total de un solo canal con datos de maniqués simulados y experimentales, y una muestra de tejido *ex vivo*. Los resultados mostraron un mejor desempeño general del método TNV para ambas estrategias, produciendo mapas ACS mejorados y extendiendo el balance entre la resolución espacial y la variabilidad de la estimación en términos de CNR con un sesgo estable.

**Palabras clave**— Ultrasonido cuantitativo, imágenes de atenuación ultrasónica, pendiente del coeficiente de atenuación, diferencia logarítmica espectral, reconstrucción conjunta, variación total, variación total nuclear, variación total Frobenius.

## Abstract

Quantitative Ultrasound (QUS) is a non-invasive image modality that characterizes numerically tissues for medical diagnosis. QUS estimators are based on acoustical parameters such as the attenuation coefficient slope (ACS). A previous study proposed denoising the spectral log ratios using a single channel total variation through frequency. The spectral-based method to estimate the ACS, known as Spectral Log Difference (SLD) does not incorporate any joint reconstruction strategies for image enhancement. Therefore, this work proposes the integration of two joint strategies compatible with the SLD framework. First, a joint regularization approach named the Total Nuclear Variation SLD (TNV-SLD) is implemented. It couples geometrical information of the ACS and the backscatter coefficient (BSC) component to enhance the quality of the images, achieving better results in terms of mean percentage error (MPE) and contrast-to-noise ratio (CNR). Later, the study is extended to jointly denoise the spectral log ratios of the SLD across the frequency channels. A multi-frequency joint method is proposed to increase the quality of the attenuation images. Two modifications of the total variation based on the Frobenius (TFV) and nuclear (TNV) norms were considered. Metrics were compared to two previous regularization methods labeled RSLD and TVSLD, based on the single-channel Total Variation with data from simulated and experimental phantoms, and an *ex vivo* tissue sample. Results showed an overall better performance of the TNV method for both strategies, yielding enhanced ACS maps and extending the trade-off between spatial resolution and variability of the estimation in terms of the CNR with a stable bias.

**Keywords**— Quantitative ultrasound, ultrasonic attenuation imaging, attenuation coefficient slope, spectral log difference, joint reconstruction, total variation, total nuclear variation, total Frobenius variation.

Dedicated to my parents for their unconditional love and support.  
To my brothers Yassir and David, who have always believed in me.  
To my entire family, teachers and friends who have helped me overcome my mistakes  
and give meaning to life.



# Acknowledgements

This thesis marks the culmination of my master's studies, and I would like to express my heartfelt gratitude to my family for their unwavering support throughout this journey. Their constant encouragement and assistance have been instrumental in enabling me to complete this work.

I extend my sincere appreciation to professors Roberto Lavarello and Benjamin Castañeda for warmly welcoming me into the Laboratorio de Imágenes Medicas (LIM) and selecting me as a Laboratory Assistant. I am grateful to the LIM members and friends Stefano Romero, Andres Coila and all the others for their invaluable support and guidance from the very beginning.

I would like to extend my sincere gratitude to Professor Adrian Basarab for his invaluable assistance and support throughout this project and his welcoming during my stay at CREATIS in Lyon, France. Additionally, I want to express my appreciation to all my other friends, colleagues, and professors I met during my Master's road who have contributed to my personal and professional growth. Their friendship and collaboration have been immensely meaningful to me.

Finally, I am deeply grateful to two funding sources. Firstly, to the Consejo Nacional de Ciencia, Tecnología e Innovación Tecnológica (CONCYTEC), for the research grant 150-2020-FONDECYT. This grant supported this study, allowing me to present my work at the 2023 IEEE International Symposium on Biomedical Imaging (ISBI) in Cartagena de Indias, Colombia, and the 2023 IEEE International Ultrasonics Symposium (IUS) in Montreal, Canada. Secondly, to the Marco Polo funding provided by the Escuela de Posgrado PUCP, which supported my visit to CREATIS in Lyon, France, in 2023.



“Saber más es ser más libre”  
Cesar Vallejo

“La vraie générosité envers l’avenir consiste à tout donner au présent”  
Albert Camus

“Reich ist man nicht durch das, was man besitzt, sondern vielmehr durch das, was man  
mit Würde zu entbehren weiß”  
Immanuel Kant

# Contents

<b>1</b>	<b>Introduction</b>	<b>1</b>
1.1	Attenuation coefficient parameter . . . . .	1
1.2	Attenuation Coefficient Slope (ACS) estimation . . . . .	1
1.2.1	Spectral Shift method . . . . .	2
1.2.2	Spectral Log Difference (SLD) method . . . . .	2
1.3	Joint reconstruction for multi-channel images . . . . .	3
1.4	Objectives . . . . .	4
1.5	Evaluation metrics . . . . .	5
1.6	Overview of the document . . . . .	6
<b>2</b>	<b>Regularized joint reconstruction for SLD</b>	<b>7</b>
2.1	Spectral Log Difference (SLD) theory . . . . .	7
2.2	Regularized Spectral Log Difference (RSLD) . . . . .	8
2.3	Total Nuclear Variation SLD (TNV-SLD) . . . . .	9
2.3.1	Algorithmic implementation . . . . .	9
2.4	Dataset . . . . .	10
2.4.1	Simulated phantom . . . . .	10
2.4.2	Tissue-mimicking phantom . . . . .	10
2.5	Reconstruction and evaluation of the ACS . . . . .	11
2.6	Results . . . . .	11
2.6.1	Simulated phantom . . . . .	11
2.6.2	Tissue-mimicking phantom . . . . .	13
2.7	Discussion . . . . .	16
<b>3</b>	<b>Multi-frequency joint reconstruction for SLD</b>	<b>17</b>
3.1	Total Variation denoising (TV) . . . . .	17
3.2	Joint Spectral Log Difference . . . . .	18
3.2.1	Total Frobenius Variation denoising (TFV) . . . . .	18
3.2.2	Total Nuclear Variation denoising (TNV) . . . . .	19
3.2.3	Algorithmic implementation . . . . .	19
3.3	Dataset . . . . .	20
3.3.1	Simulated data . . . . .	20
3.3.2	Experimental phantom . . . . .	20
3.3.3	<i>Ex vivo</i> tissue . . . . .	20
3.4	Reconstruction and evaluation of the ACS . . . . .	21
3.5	Results . . . . .	22



3.5.1	Simulated phantom . . . . .	22
3.5.2	Experimental phantom . . . . .	23
3.5.3	Ex Vivo Tissue . . . . .	26
3.6	Discussion . . . . .	26
<b>4</b>	<b>Conclusions</b>	<b>29</b>
	<b>Bibliography</b>	<b>30</b>



# List of Figures

2.1	ACS maps when using the (a)-(c) RSLD and (f)-(h) TNV-SLD techniques for data block sizes of $10\lambda \times 10\lambda$ , $20\lambda \times 20\lambda$ , $30\lambda \times 30\lambda$ for the simulated phantom. The black lines outline the regions for calculation metrics. . . . .	11
2.2	MPE at different block sizes in the (a) inclusion and (b) background regions for the simulated phantom. . . . .	12
2.3	(a) MPE, (b) CNR of the ACS for the simulated phantom with the RSLD and TNV-SLD methods, cases with maximum CNR are marked. . . . .	13
2.4	ACS maps when using the (a)-(e) RSLD and (f)-(j) TNV-SLD techniques for data block sizes of $10\lambda \times 10\lambda$ , $20\lambda \times 20\lambda$ , $30\lambda \times 30\lambda$ for the tissue-mimicking phantom. The black lines outline the regions for calculation metrics. . . . .	14
2.5	MPE at different block sizes in the (a) inclusion and (b) background regions for the tissue-mimicking phantom. . . . .	15
2.6	(a) MPE, (b) CNR of the ACS for the simulated phantom with the RSLD and TNV-SLD methods, cases with maximum CNR are marked. . . . .	15
3.1	Workflow showing the reconstruction of the ACS maps from the denoised spectral ratios. . . . .	21
3.2	ACS maps generated for the simulated phantom when using (b-e) TV, (c-f) TFV and (d-g) TNV techniques, respectively. The lines outline the regions for metrics . . . . .	22
3.3	CNR of the ACS maps using the TV, TFV and TNV techniques at different block sizes for the simulated phantom. . . . .	23
3.4	ACS maps generated for the experimental phantom when using (b-e) TV, (c-f) TFV, and (d-g) TNV techniques, respectively. The lines outline the regions for metrics. . . . .	24
3.5	CNR of the ACS maps using the TV, TFV and TNV techniques at different block sizes for the experimental phantom. . . . .	24
3.6	(a) Average MPE of both regions, (b) CNR of the experimental phantom with the TV, TFV and TNV methods for a data block size of $20\lambda$ . The optimal range of $\mu$ is identified by minimizing the MPE denoted by the vertical dashed lines. . . . .	25
3.7	ACS maps generated for the <i>ex vivo</i> porcine tissue with $10\lambda$ with and $20\lambda$ when using (b-e) TV, (c-f) TFV and (d-g) TNV techniques, respectively. The lines outline the regions for metrics. . . . .	27
3.8	CNR of the ACS maps using the TV, TFV and TNV techniques at different block sizes for the <i>ex vivo</i> porcine tissue. . . . .	28

# List of Tables

2.1	MPE, CV and CNR of the final ACS maps with RSLD and TNV-SLD for the simulated phantom at different block sizes. Ground-truth values $1 \text{ dB}\cdot\text{cm}^{-1}\cdot\text{MHz}^{-1}$ (inclusion) and $0.5 \text{ dB}\cdot\text{cm}^{-1}\cdot\text{MHz}^{-1}$ (background). . . . .	12
2.2	MPE, CV and CNR of the final ACS maps with RSLD and TNV-SLD for the tissue-mimicking phantom at different block sizes. Ground-truth values $1.04 \text{ dB}\cdot\text{cm}^{-1}\cdot\text{MHz}^{-1}$ (inclusion) and $0.54 \text{ dB}\cdot\text{cm}^{-1}\cdot\text{MHz}^{-1}$ (background). . . . .	14
3.1	Comparison of mean, std, MPE, SDPE and CNR for the ACS maps of the simulated phantom using the proposed joint reconstruction techniques (TFV and TNV) and TV. Ground-truth values $1 \text{ dB}\cdot\text{cm}^{-1}\cdot\text{MHz}^{-1}$ (inclusion) and $0.5 \text{ dB}\cdot\text{cm}^{-1}\cdot\text{MHz}^{-1}$ (background). . . . .	23
3.2	Comparison of mean, std, MPE, SDPE and CNR for the ACS maps of the experimental phantom using the proposed joint reconstruction techniques (TFV and TNV) and TV. Ground-truth values $0.97 \text{ dB}\cdot\text{cm}^{-1}\cdot\text{MHz}^{-1}$ (inclusion) and $0.55 \text{ dB}\cdot\text{cm}^{-1}\cdot\text{MHz}^{-1}$ (background). . . . .	25
3.3	Comparison of mean, std and CNR for the ACS maps of the <i>ex vivo</i> porcine tissue using the proposed joint reconstruction techniques (TFV and TNV) and TV . . . . .	26

# Chapter 1

## Introduction

Ultrasound is a noninvasive imaging modality that uses sound waves of frequencies higher than the range of human hearing, i.e.  $f > 20\text{KHz}$  for tissue characterization. Although current ultrasound technologies are well capable of identifying suspicious lesions, they only provide qualitative information of tissues, therefore the diagnosis of a benign or malignant tissue is subject to the interpretation of the clinician [1]. In contrast, quantitative ultrasound (QUS) techniques have been developed to characterize tissues objectively based on their macroscopic [2]. QUS has been proven to be an effective diagnostic tool for breast cancer detection [3], thyroid cancer diagnosis [4], liver disease quantification [5] and monitoring the state of tendons after surgery [6].

### 1.1 Attenuation coefficient parameter

QUS techniques analyze the radio-frequency (RF) data and provide numerical values of tissue properties by estimating acoustical parameters such as the backscatter coefficient (BSC) and the attenuation coefficient slope (ACS). The BSC measures the scattering and wave reflection due to interference inside the tissue, in physics terms, it corresponds to the scattered intensity in the backward direction per unit solid angle  $\text{cm}^{-1} \cdot \text{Sr}^{-1}$ . Information of the BSC has been used in clinical studies for breast tumors, liver pathologies, and thyroid cancer [7]. Nevertheless, the estimation of the BSC requires an attenuation compensation through the propagation path and it is affected by the ACS precision [8].

On the other hand, the attenuation coefficient is related to the loss of mechanical energy as the ultrasonic waves propagate through the tissue and it increases with frequency. This dependency is typically assumed to be linear, therefore, it is common to report attenuation by calculating its slope or ACS expressed in  $\text{dB} \cdot \text{cm}^{-1} \cdot \text{MHz}^{-1}$  [9]. Attenuation imaging has shown promise for the assessment of liver diseases [10]. Furthermore, the attenuation estimation has been proven to be related to the precision of other acoustical parameters estimation such as the backscatter coefficient [11].

### 1.2 Attenuation Coefficient Slope (ACS) estimation

The methods to assess the ACS are based on the spectral information from the RF backscattered echoes, they measure the central frequency downshift in the spectrum

(spectral shift methods) or the logarithmic intensity decay at each frequency (spectral log difference methods) [9].

### 1.2.1 Spectral Shift method

In the Spectral Shift method, the attenuation is calculated from the downshift of the ultrasound central frequency at different depths. It was initially proposed in 1983 by Fink et al. [12] who recovered the downshift using a short-time Fourier analysis technique. Other estimators to locate the center frequency are based on 1) a correlation analysis with a set of templates generated by calculating the spectrum of the known ultrasound pulse, 2) a mean frequency approach considering a Gaussian-shaped spectrum and 3) a zero-crossing method by counting the number of zero values in a given interval of time and dividing it to the number of samples [13]. Later, Baldeweck et al. [14] proposed a second-order auto-regressive model to reduce the variance of estimations with computational efficiency. More recently, Samini and Varghese [15] presented an optimum frequency shift estimator that reduced three times the standard deviation of the ACS in comparison to current shift methods, using a reference phantom similar to the spectral log difference technique. Common limitations of spectral shift techniques are the sensitivity to local spectral noise artifacts and the difficulty in compensating and correcting diffraction effects in comparison to spectral difference methods [16].

### 1.2.2 Spectral Log Difference (SLD) method

The Spectral Log Difference (SLD) formulation dates back to 1990, when Xin Yao et al. [17] proposed comparing the echo sample data with a reference calibrated phantom to estimate the backscatter and attenuation coefficients. The SLD assumes a linear dependence between frequency and uses fitting tools to calculate the ACS from the log ratio of the power spectra of the proximal and distal segments of a certain region of interest (ROI) [18]. Due to the large variability of estimations using a typical SLD, regularization techniques have been proposed. The first regularized SLD (RLSD) approach was developed in [19] and reduced the estimations variability by around 90% by incorporating a generalized Tikhonov regularization approach, testing their model in a homogeneous phantom and improving the quality of the attenuation maps.

The study was extended in [20], where the isotropic total variation (TV) was proposed as a new regularization term by assuming physical structures to be piecewise homogeneous within the medium. The minimization problem was achieved by using the scaled alternating direction method of multipliers (ADMMs), reporting accurate and precise attenuation estimations in simulations, phantoms and *in vivo* breast tissue. The RLSD technique has been validated in human thyroid *in vivo* with Hashimoto's thyroiditis, adenomatoid nodules, and papillary carcinoma showing similar results with the reported values in the literature [21]. Furthermore, Saavedra et al. [22] presented a multi-wave quantitative ultrasound to study skin *in vivo* by incorporating the ACS obtained by RLSD with the shear wave speed (SWS) from crawling wave sonoelastography (CrW), suggesting the estimators can be applied for a more robust a complete skin characterization. Results have shown the RLSD approach overcomes the well-known trade-off of SLD between the precision of the ACS and the data block size used in the spectral-based

technique, although the limitation of the method corresponds to the sensitivity of the regularization term in the ACS estimation.

A spatial modification of the TV regularization term was proposed by Deeba et al. [23], the new method modulated the signal-to-noise-ratio deviation as an indicator of tissue heterogeneity for a new spatially weighted regularization term with better accuracy and precision. Nevertheless, no structural similarities between the BSC and ACS within the medium were exploited and both terms were considered isolated channels in the optimization problem. Another approach of spatial regularization was proposed in [24], where the SLD problem was solved by proposing a denoising prior based on a single-channel TV across the frequencies of the spectral log ratios, labeled as TVSLD. Results showed attenuation maps with greater CNR, nevertheless, no structure similarities among the frequency channels were exploited, since they were also considered independent channels, and non-joint reconstruction techniques were developed.

In summary, SLD techniques have shown great potential for improving medical diagnosis, by detecting several diseases. Current approaches have used regularization techniques to solve the ACS as an isolated inverse problem. Nevertheless, results showed ACS estimations with high variability, hence research is still required to enhance the precision. The goal is to reduce the ACS variability and improve the quality of the image by coupling information of other channels as the BSC term or spectral ratios across the frequency, using joint or synergistic reconstruction techniques using joint or synergistic reconstruction techniques. By coupling information from different channels structure similarities can be exploited in order to reconstruct ACS maps jointly with less variability and higher quality in comparison to reconstructing them independently.

### 1.3 Joint reconstruction for multi-channel images

In recent years, great strides have been made in the development of joint/synergistic reconstruction techniques that leverage intrinsic properties across channels to reconstruct and enhance multi-channel or vector images [25]. The techniques can be grouped according to the approach used to couple the channels, an overview of the state-of-the-art is presented following the nomenclature given in [26]. An initial point to define a synergistic image reconstruction relies on formulating the inverse problem as a joint maximum *a posteriori* (JMAP) estimate, whose general obstacle is how to select a suitable multi-modality likelihood [27]. To overcome this limitation, a certain conditional prior must be assumed. For instance, when the application aims to promote a joint sparsity among channels, a common approach is to choose the joint total variation as a regularization term, also known as Vectorial Total Variation (VTV) in the image processing field. Since MR images are piecewise smooth, therefore their gradients are close to zero, the VTV was used for a calibrationless Parallel MRI (pMRI) outperforming other state-of-the-art pMRI techniques [28]. Moreover, the joint total variation was used in multi-contrast MRI with partially sample K-space data to achieve more accurate reconstructions [29].

In cases where the objective is to establish a coherent structure among the channels, joint reconstruction approaches such as the Parallel Level Sets (PLS) prior, which analyzes the direction of gradients and their parallelism, are employed. PLS is not affected by different scales in channels and thus is not affected by different scales in channels and

was tested to jointly reconstruct MR and PET images enhancing common anatomical boundaries and preserving unique features with fewer artifacts [30, 31]. A generalization of PLS approach was introduced for multi-channel X-ray computed tomography to encourage joint smoothing directions and obtain higher quality reconstructions [32].

A similar approach is the Total Nuclear Variation (TNV) which encourages joint sparsity and directional alignment of the gradient vectors (or the Jacobian) with the advantage of being convex in comparison to PLS [33]. TNV was explored for reconstructing multi-channel spectral CT images to encourage edge location and a shared gradient among image channels and preserving features at high values of regularization [34]. The technique was extended and applied to real dual-energy CT data, comparing to a TV and a Frobenius norm, final results showed the TNV outperformed the other methods, leading to more accurate and enhanced images when denoising multi-channel images [35].

Another approach is based on joint statistics, in [36] an entropy analysis based on wavelets was used to incorporate high-resolution anatomical information (from MR or CT) in PET image reconstruction, achieving improved noise reduction while maintaining comparable regional mean values in simulation and clinical cases. Moreover, in MR images the correlation between different T1- and T2-weighted images can be exploited to promote sparsity, for better joint reconstruction results with fewer K-space samples [37]. Additionally, dictionary-learning methods can be extended to improve PET and MRI reconstructions using sparse dictionaries capable of capturing image texture, showing better qualitative and quantitative results for both modalities [38]. Lastly, there has been an increasing trend toward learning-based methods for image processing, introducing a deep convolutional neural network (CNN) prior for denoising in MRI reconstructions [39]. The well-known U-Net architecture has been adapted as a two-channel reconstruction method in ultrasound tomography. [40]. Nevertheless, a common limitation of this kind of approach relates to the scarcity of robust datasets [26].

All in all, joint reconstruction methods have shown promise to enhance image quality in comparison to single channel/modality techniques. These methods leverage structure similarities across multiple channels, allowing for the joint reconstruction of images with reduced variability. This work develops two approaches for joint reconstruction in QUS. Firstly, TNV was introduced to address the SLD as an inverse problem by integrating information from the ACS and a constant BSC term. Secondly, two variations of the Total Variation (TV) norm, specifically the Frobenius and nuclear norms, were used to couple information from different frequencies during the denoising process of the spectral log ratios. Both approaches were implemented using the Primal-Dual Splitting algorithm [41]. The joint methods achieved an improved trade-off between the spatial resolution and variability of the reconstructed attenuation images without degrading the accuracy compared to previous single-channel TV-based techniques.

## 1.4 Objectives

The main objective of this work is to develop novel joint reconstruction methods that leverage the Spectral Log Difference (SLD) framework for accurate estimation of the attenuation coefficient slope in quantitative ultrasound images. The specific objectives of this work are:

- To use joint reconstruction techniques based on Total Frobenius Variation and Total Nuclear Variation for the design of a coupled method for ultrasonic attenuation imaging
- To implement and test the joint reconstruction techniques with data obtained from simulations, experimental phantoms, and *ex vivo* tissue data.
- To compare the performance of the implemented joint reconstruction method with other state-of-the-art methods in terms of estimation error, variability, and contrast to noise ratio.

## 1.5 Evaluation metrics

To compare the performance of the implemented reconstruction methods, metrics of the estimated ACS values such as mean, standard deviation, mean percentage error (MPE) and its standard deviation (SDPE), and Contrast-to-Noise Ratio (CNR) were calculated. The formal definitions of the mentioned metrics are detailed below [24].

- Statistical metrics: Such as mean ( $\bar{x}$ ), standard deviation ( $\sigma$ ) and coefficient of variation (CV) the estimated ACS.
- Mean Percentage Error (MPE) to estimate the bias in the background and inclusion regions

$$MPE = \frac{1}{Q} \sum_{i,j} \frac{\beta_{i,j} - \beta_{i,j}^o}{\beta_{i,j}^o} \quad (1.1)$$

- Standard Deviation Percentage Error (SDPE) to estimate the variability of the estimations in the background and inclusion regions

$$SDPE = \sqrt{\frac{1}{Q} \sum_{i,j} \left( \frac{\beta_{i,j} - \beta_{i,j}^o}{\beta_{i,j}^o} \right)^2} - MPE \quad (1.2)$$

- Contrast to noise ratio (CNR) to evaluate the quality of the ACS map

$$CNR = \frac{|\bar{x}_{inc} - \bar{x}_{back}|}{\sqrt{\sigma_{inc}^2 + \sigma_{back}^2}}, \quad (1.3)$$

where  $\beta$  and  $\beta^o$  are the estimated and ground truth ACS values, respectively,  $Q$  is the number of pixels in the region of metrics, and  $\bar{x}$  and  $\sigma$  correspond to the mean and standard deviation of the ACS values within the inclusion (*inc*) and background (*back*).



## 1.6 Overview of the document

**Chapter 2, Regularized joint reconstruction for SLD** describes the fundamentals of the SLD method and the regularization approach to obtain the ACS as an inverse problem [19] and proposes a joint reconstruction method labeled the Total Nuclear Variation SLD (TNV-SLD). This method couples the geometrical information of the ACS and the backscatter component to enhance the quality of the images. This approach was presented at the 2023 IEEE ISBI conference [42].

**Chapter 3, Multi-frequency joint reconstruction for SLD** proposes a joint method by coupling information from different frequencies when denoising the spectral log ratios, exploiting structure similarities using the weighted Frobenius and the weighted nuclear variation, providing a good balance between noise removal and preservation of edges and textures. This approach was presented at the 2023 IEEE IUS conference [43].

**Chapter 4, Conclusions** summarizes the final conclusions of both strategies.



# Chapter 2

## Regularized joint reconstruction for SLD

This chapter will explain the basic theory of the spectral log difference technique, the replication stage for the non-joint Regularized Spectral Log Difference proposed by Coila et al. [20], and the fundamentals of the new Total Nuclear Variation approach for joint regularization.

### 2.1 Spectral Log Difference (SLD) theory

In pulse-echo ultrasound, the power spectrum of a local region, i.e. block can be modeled by [18]

$$S_s(x, z, f) = P(f)D_s(x, z, f)BSC_s(x, z, f)A_s(x, z_0, f) e^{-4\alpha_s(x, z, f)(z-z_0)}, \quad (2.1)$$

where  $z$  denotes the spatial dimension along the ultrasound wave propagation (axial),  $x$  represents the lateral dimension, and  $f$  indicates the frequency axis.  $P(f)$  denotes the scanner transfer function which is considered spatially invariant within a block,  $D_s(x, z, f)$  represents the diffraction effects,  $A_s(x, z, f)$  is the cumulative attenuation from the transducer to the upper limit  $z_0$  of the block, and  $BSC_s(x, z, f)$  and  $\alpha_s(x, z, f)$  are the backscatter and attenuation coefficients, respectively.

The SLD technique involves splitting a range gate (data-block) into two sub-blocks of equal axial length, at a proximal and distal depth defined as  $z_p = z - \Delta z$  and  $z_d = z + \Delta z$ , respectively [20]. The logarithmic ratio of the power spectrum of the proximal  $S_s(x, z_p, f)$  and distal  $S_s(x, z_d, f)$  windows can be expressed as

$$Y(x, z, f) \triangleq \ln \left[ \frac{S_s(x, z - \Delta z, f)}{S_s(x, z + \Delta z, f)} \cdot \frac{D_s(x, z + \Delta z, f)}{D_s(x, z - \Delta z, f)} \right], \quad (2.2)$$

$$Y(x, z, f) = 4L\alpha_s(x, z, f) + \ln \left[ \frac{BSC_s(x, z - \Delta z, f)}{BSC_s(x, z + \Delta z, f)} \right], \quad (2.3)$$

where  $L = z_d - z_p$ . For array transducers, the  $D_s(x, z, f)$  term is compensated by using a homogeneous reference phantom, therefore the diffraction ratio is estimated as

$$\frac{D_s(x, z + \Delta z, f)}{D_s(x, z - \Delta z, f)} \approx \frac{S_r(x, z + \Delta z, f)}{S_r(x, z - \Delta z, f)} e^{4L\alpha_r(x, z, f)}, \quad (2.4)$$

where  $S_r(x, z, f)$  represents the power spectra of the reference and  $\alpha_r(x, z, f)$  is the attenuation coefficient of the medium. Finally, Eq. (2.2)-(2.3) are rewritten as

$$Y(x, z, f) \triangleq \ln \left[ \frac{S_s(x, z - \Delta z, f)}{S_r(x, z - \Delta z, f)} \cdot \frac{S_r(z + \Delta z, f)}{S_s(z + \Delta z, f)} \right] + 4L\alpha_r(x, z, f), \quad (2.5)$$

$$Y(x, z, f) = 4L\beta(x, z)f + c, \quad (2.6)$$

where  $c = \ln [BSC_s(x, z - \Delta z, f)/(BSC_s(x, z + \Delta z, f))]$  with  $c$  not varying with  $x$ ,  $z$ , or  $f$  and  $\beta(x, z)$  corresponds to the ACS to be estimated.

The discretized model is formulated by considering a grid with points along the lateral, axial and frequency axes, represented by  $i$ ,  $j$  and  $k$ , respectively. Here,  $m$ ,  $n$  and  $p$  represent the total number of points along each axis.

$$Y_{i,j,k} = 4L\beta_{i,j}f_k + c, \quad (2.7)$$

with  $i \in \{1, 2, \dots, m\}$ ,  $j \in \{1, 2, \dots, n\}$  and  $k \in \{1, 2, \dots, p\}$ . The ACS denoted by  $\beta$  is typically estimated using linear regression [44].

## 2.2 Regularized Spectral Log Difference (RSLD)

The RLSD technique [20] was the first method to incorporate regularization in the SLD framework and compensate for the trade-off between precision and spatial resolution. First, Eq. 2.6 is rewritten in a matrix form assuming Gaussian noise, denoted by  $\eta$

$$\begin{bmatrix} \mathbf{y} \end{bmatrix}_{mnp \times 1} = \begin{bmatrix} \mathbf{A} \end{bmatrix}_{mnp \times 2mn} \cdot \begin{bmatrix} \mathbf{B} \\ \mathbf{C} \end{bmatrix}_{2mn \times 1} + \eta \rightarrow \mathbf{y} = \mathbf{A}\mathbf{x} + \eta, \quad (2.8)$$

where  $\mathbf{y} \in \mathbb{R}^{mnp \times 1}$  is the vectorized form of  $Y$ . The vector  $\mathbf{x} = [\mathbf{B} \ \mathbf{C}]^T \in \mathbb{R}^{2mn \times 1}$  contains the values of  $\beta$  and  $c$  in a concatenated form, where  $\mathbf{B}$  and  $\mathbf{C}$  are the individual vectors. Additionally, the matrix  $\mathbf{A} \in \mathbb{R}^{mnp \times 2mn}$  establishes the relationship between  $\mathbf{y}$  and the unknown vectors  $\mathbf{B}$  and  $\mathbf{C}$ . Later, Eq. 2.8 is solved as a 2-D inverse problem as follows

$$\arg \min_{\mathbf{x}} \frac{1}{2} \|\mathbf{y} - \mathbf{A}\mathbf{x}\|_2^2 + \mu \mathcal{R}(\mathbf{x}) = \arg \min_{\mathbf{x}} f(\mathbf{x}), \quad (2.9)$$

$$\mathcal{R}(\mathbf{x}) \triangleq \text{TV}(\mathbf{B}) + \text{TV}(\mathbf{C}), \quad (2.10)$$

where  $\frac{1}{2} \|\mathbf{y} - \mathbf{A}\mathbf{x}\|_2^2$  is the fidelity term based on the  $\ell_2$ -norm,  $\mu$  is the regularization parameter and  $\mathcal{R}(\mathbf{x})$  is the regularization term. Under the assumption of a piece-wise homogeneous medium the isotropic total variation (TV) is selected and applied independently to the  $\beta$  and  $c$  channels.

## 2.3 Total Nuclear Variation SLD (TNV-SLD)

As previously mentioned, coupling information of different channels reconstructs images with less variability in different modalities. In particular, the Total Nuclear Variation (TNV) is selected as a new regularization term. This technique is based on geometrical structure constraints among channels and is defined as

$$\text{TNV}(\mathbf{x}) = \|\mathcal{J}(\mathbf{x})\|_{1,*} = \sum_{i,j}^{m,n} \|\mathcal{J}(\mathbf{x})\|_*, \quad (2.11)$$

where  $\mathcal{J}(\mathbf{x})$  is the discrete Jacobian [34, 35, 45] of the multi-channel image  $\mathbf{x}$ , formed by the gradients in the lateral  $\nabla_x$  and axial  $\nabla_z$  directions,  $\|\cdot\|_*$  is referred to as the nuclear norm and is calculated by the sum of its singular values (i.e.  $\|Z\|_* = \sum_r \sigma_r(Z)$ ). For this case,  $\mathcal{J}(\mathbf{x})$  is defined as follows

$$\mathcal{J}(\mathbf{x}) = \begin{bmatrix} \nabla_x(\mathbf{B}) & \nabla_x(\mathbf{C}) \\ \nabla_z(\mathbf{B}) & \nabla_z(\mathbf{C}) \end{bmatrix}^T, \quad (2.12)$$

Finally, the problem in Equation 2.9 considering TNV is rewritten as

$$\arg \min_{\mathbf{x}} \frac{1}{2} \|\mathbf{y} - A\mathbf{x}\|_2^2 + \mu \text{TNV}(\mathbf{x}), \quad (2.13)$$

in this case, TNV-SLD assumes the two channels of  $\mathbf{x}$ :  $\mathbf{B}$  (related to ACS) and  $\mathbf{C}$  (related to BSC) will share structure similarities in the same medium by coupling their edges and aligning their gradients.

### 2.3.1 Algorithmic implementation

The solution that minimizes the Eq. 2.13 can be achieved by the Primal-Dual Splitting method [41]. First, TNV is expressed using the definition of dual-norm and an auxiliary variable  $z$

$$\text{TNV}(\mathbf{x}) = \sum_{i,j}^{m,n} \|\mathcal{J}(\mathbf{x})\|_* = \max_z \langle \mathcal{J}(\mathbf{x}), z \rangle, \quad \text{s.t. } \sigma_{max}(z) \leq 1 \quad (2.14)$$

with  $\sigma_{max}$  as the maximum singular value, Eq. 2.14 is equivalent to

$$\text{TNV}(\mathbf{x}) = \max_z \langle \mathcal{J}(\mathbf{x}), z \rangle - \delta_{\mathcal{N}}(z), \quad \text{with } \mathcal{N} = \{z : \sigma_{max} \leq 1\} \quad (2.15)$$

where  $\langle \cdot, \cdot \rangle$  is the inner product,  $\delta_{\mathcal{N}}(z)$  is the well-known indicator function. Hence, combining Equations 2.13 and 2.15 the cost function is expressed as

$$\arg \min_{\mathbf{x}} \max_z \frac{1}{2} \|\mathbf{y} - A\mathbf{x}\|_2^2 - \mu \delta_{\mathcal{N}}(z) + \mu \langle \mathcal{J}(\mathbf{x}), z \rangle, \quad (2.16)$$

$$\arg \min_{\mathbf{x}} \max_z G(\mathbf{x}) - H^*(z) + \langle L(\mathbf{x}), z \rangle, \quad (2.17)$$

Finally, the convex optimization problem can be resolved with proximal operators, following the algorithm proposed by Condat [41].

---

**Algorithm 1** Primal-Dual Splitting Algorithm

---

$$G(\mathbf{x}) = \frac{1}{2}\|\mathbf{y} - A\mathbf{x}\|_2^2, \quad H^*(z) = \mu\delta(z), \quad L(\mathbf{x}) = \mathcal{J}(\mathbf{x})$$

**repeat**  
     $\hat{\mathbf{x}}_{n+1} := \text{prox}_{\tau G}(\mathbf{x}_n - \tau L^*(z_n))$   
     $\hat{z}_{n+1} := \text{prox}_{\sigma H^*}(z_n + \sigma L(2\hat{\mathbf{x}}_{n+1} - \mathbf{x}_n))$   
     $(\mathbf{x}_{n+1}, z_{n+1}) := \rho(\hat{\mathbf{x}}_{n+1}, \hat{z}_{n+1}) + (1 - \rho)(\mathbf{x}_n, z_n)$   
**until**  $\frac{\|f(\mathbf{x}_{n+1}) - f(\mathbf{x}_n)\|_2}{\|f(\mathbf{x}_n)\|_2} < \epsilon$ ; convergence criteria

---

The proximal operators used in the algorithm are defined as follows

$$\text{prox}_{\tau G}(x) = (I + \tau A^* A)^{-1}(x + \tau A^* \mathbf{y}), \quad (2.18)$$

$$\text{prox}_{\sigma H^*}(x) = x - \sigma \text{prox}_{H/\sigma}(x/\sigma), \quad (2.19)$$

where the  $I$  is the identity matrix. The first proximal operator corresponds to the classical case of  $\ell_2$ -norm of the fidelity term [46] and the second operator is obtained thanks to Moreau's identity, where  $\text{prox}_{H/\sigma}$  consists in a soft-thresholding process of the singular values ( $\tilde{\sigma}_k = \max(\sigma_k - \mu, 0)$ ). The  $\tau, \sigma$  and  $\rho$  are relaxation and proximal parameters related to the convergence speed of the algorithm. The impact of their value has been studied extensively in [46], suggesting practical criteria of  $\sigma = (\rho - 0.5\tau)/8\tau$ ,  $\rho \approx 1.99$ . Lastly,  $\tau$  can be achieved by grid search inspection, for this case  $\tau = 0.01$  was considered.

## 2.4 Dataset

### 2.4.1 Simulated phantom

A simulated phantom was generated with the k-Wave toolbox [47] in MATLAB. The simulation contained a circular inclusion with a 20 mm diameter with a 6.66 MHz linear transducer with 0.3 mm pitch and 128 elements. The ACS ideal values for the background and inclusion were defined as 0.5 and 1  $\text{dB}\cdot\text{cm}^{-1}\cdot\text{MHz}^{-1}$ , respectively. The diffraction was compensated with a simulated homogeneous phantom with an ACS of 0.3  $\text{dB}\cdot\text{cm}^{-1}\cdot\text{MHz}^{-1}$ .

### 2.4.2 Tissue-mimicking phantom

Experimental data from a tissue-mimicking phantom reported in [20] was used. Data acquisition was performed using a micropositioning system controlled by custom LabVIEW software (National Instruments, Austin, TX, USA) and a 7.5 MHz (f/4) single-element transducer driven by an Olympus Panametrics 5900 pulser/receiver. The phantom had a cylindrical shape of 70 mm diameter background with a 25 mm diameter inclusion. The ground truth ACS values were found to be 0.54  $\text{dB}\cdot\text{cm}^{-1}\cdot\text{MHz}^{-1}$  and 1.04  $\text{dB}\cdot\text{cm}^{-1}\cdot\text{MHz}^{-1}$  for the background and inclusion, respectively.

## 2.5 Ronstruction and evaluation of the ACS

The ACS maps were generated using block sizes of  $10\lambda \times 10\lambda$ ,  $20\lambda \times 20\lambda$ ,  $30\lambda \times 30\lambda$ ,  $40\lambda \times 40\lambda$  and  $50\lambda \times 50\lambda$  ( $\lambda$  represents the wavelength) an overlap of 80% and a bandwidth of 3-9 MHz, considering a decay of the spectrum of 20 dB. Metrics of the inclusion and background regions as mean percentage error (MPE) and contrast-to-noise ratio (CNR) were calculated using the RSLD and TNV-SLD techniques. In order to compare the robustness of both methods, the metrics were calculated for different values of the regularization parameter  $\mu$  as powers of 10. The ACS maps presented were constructed with the  $\mu$  values that maximized the CNR of the image.

## 2.6 Results

### 2.6.1 Simulated phantom

Metrics of the inclusion and background regions as MPE, CV, and CNR were calculated using the RSLD and TNV-SLD techniques and synthesized in Table 2.1 and the obtained MPE for the inclusion and background at different block sizes are displayed in Fig. 2.2. The ACS maps at different block sizes with RSLD ( $\mu = 10^4$ ) and TNV-SLD ( $\mu = 10^4$ ) are presented in Fig. 2.1.

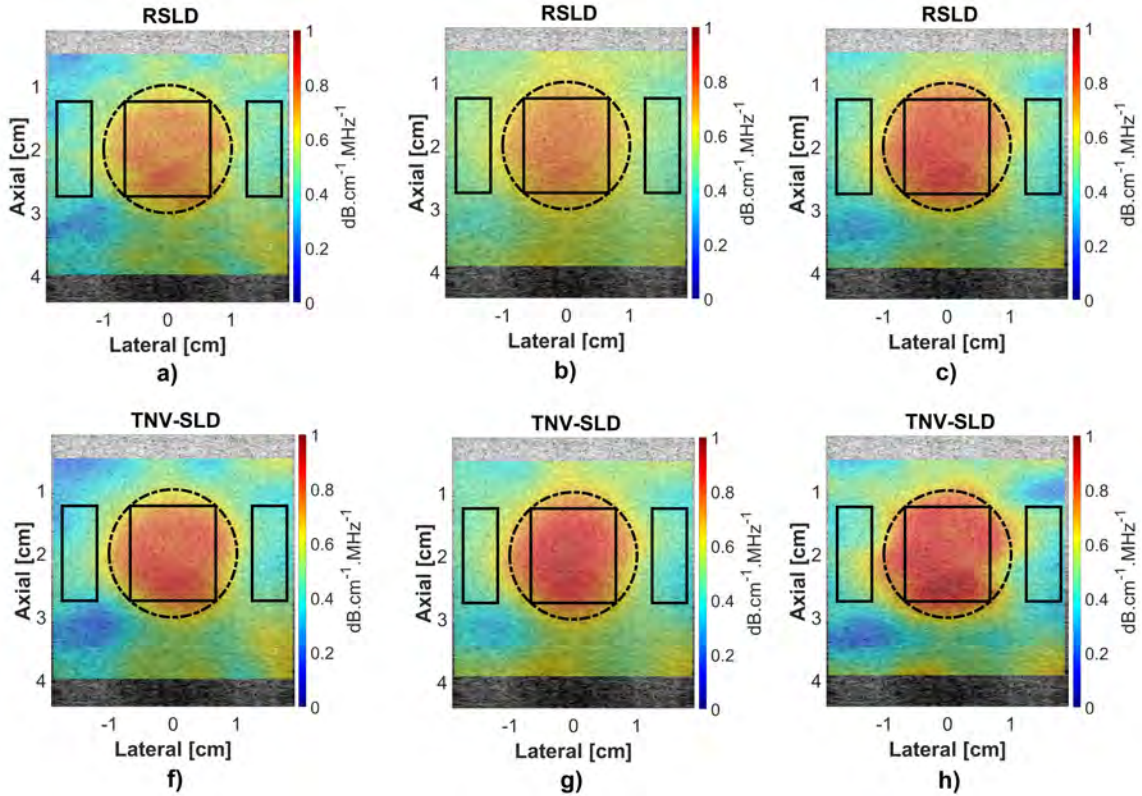


Figure 2.1: ACS maps when using the (a)-(c) RSLD and (f)-(h) TNV-SLD techniques for data block sizes of  $10\lambda \times 10\lambda$ ,  $20\lambda \times 20\lambda$ ,  $30\lambda \times 30\lambda$  for the simulated phantom. The black lines outline the regions for calculation metrics.

Table 2.1: MPE, CV and CNR of the final ACS maps with RSLD and TNV-SLD for the simulated phantom at different block sizes. Ground-truth values  $1 \text{ dB}\cdot\text{cm}^{-1}\cdot\text{MHz}^{-1}$  (inclusion) and  $0.5 \text{ dB}\cdot\text{cm}^{-1}\cdot\text{MHz}^{-1}$  (background).

Block Size	Technique	$\mu$	Inclusion		Background		CNR
			MPE	CV	MPE	CV	
$10\lambda$	RSLD [20]	$10^{3.5}$	25.82	6.06	5.65	11.6	3.47
	TNV-SLD	$10^{3.5}$	<b>19.69</b>	6.84	<b>2.56</b>	15.27	3.29
$20\lambda$	RSLD [20]	$10^4$	25.44	5.10	8.11	14.99	3.13
	TNV-SLD	$10^4$	<b>15.86</b>	7.44	<b>2.84</b>	15.01	3.13
$30\lambda$	RSLD [20]	$10^{3.5}$	17.96	5.38	3.66	14.63	3.26
	TNV-SLD	$10^{3.5}$	<b>15.7</b>	5.55	<b>2.82</b>	16.53	3.23
$40\lambda$	RSLD [20]	$10^{3.5}$	16.46	4.83	17.30	10.18	3.23
	TNV-SLD	$10^{3.5}$	<b>14.47</b>	5.18	<b>16.90</b>	11.34	3.19
$50\lambda$	RSLD [20]	$10^{3.5}$	19.93	5.43	17.56	8.91	2.91
	TNV-SLD	$10^{3.5}$	<b>18.53</b>	5.74	<b>17.33</b>	9.44	2.90

The results show clear differences between the RSLD and TNV-SLD techniques, particularly evident in the MPE values and CNR metrics across varying block sizes. This highlights how TNV-SLD achieved ACS images with better quality and accuracy.

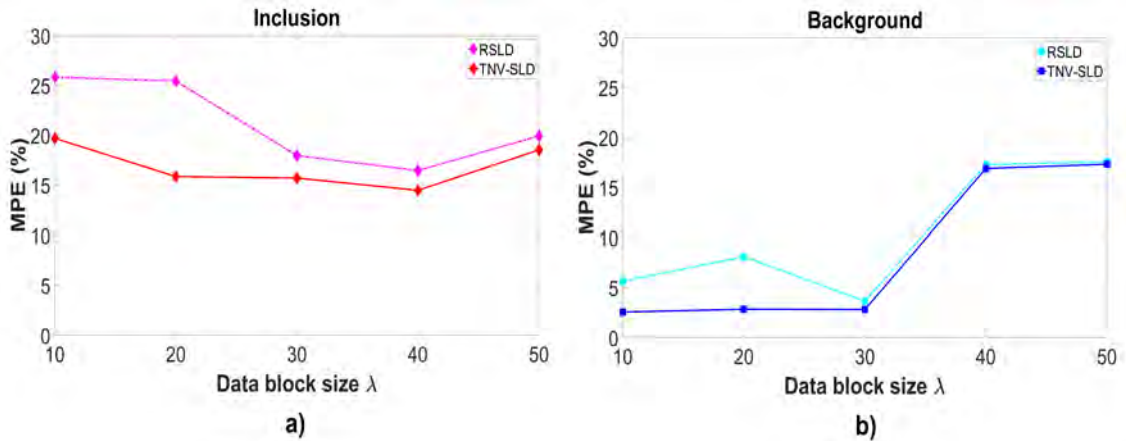


Figure 2.2: MPE at different block sizes in the (a) inclusion and (b) background regions for the simulated phantom.

### Impact of the regularization parameter

In order to compare the robustness of both methods, the metrics were calculated for different values of the regularization parameter  $\mu$  as powers of 10. The impact of the  $\mu$  value was evaluated in terms of MPE and CNR, particular case using a fixed data block size of  $20\lambda \times 20\lambda$  is presented in Fig. 2.3. This analysis reveals how the choice of  $\mu$  influences the performance of both RSLD and TNV-SLD techniques, with the latter demonstrating better robustness and consistency across a range of values.

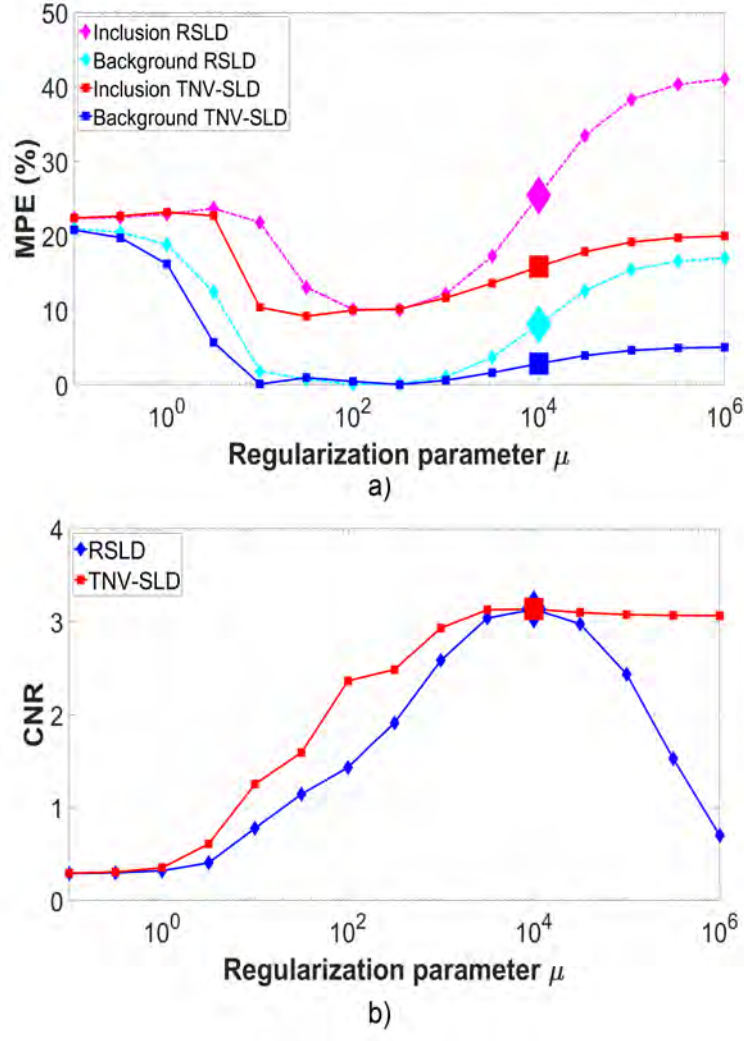


Figure 2.3: (a) MPE, (b) CNR of the ACS for the simulated phantom with the RSLD and TNV-SLD methods, cases with maximum CNR are marked.

## 2.6.2 Tissue-mimicking phantom

Metrics of the inclusion and background regions as MPE, CV and CNR were calculated using the RSLD and TNV-SLD techniques and synthesized in Table 2.2 and the obtained MPE for the inclusion and background at different block sizes are displayed in Fig. 2.5. The ACS maps at different block sizes reconstructed with RSLD ( $\mu = 10^{4.5}$ ) and TNV-SLD ( $\mu = 10^{5.5}$ ) are presented in Fig. 2.4.



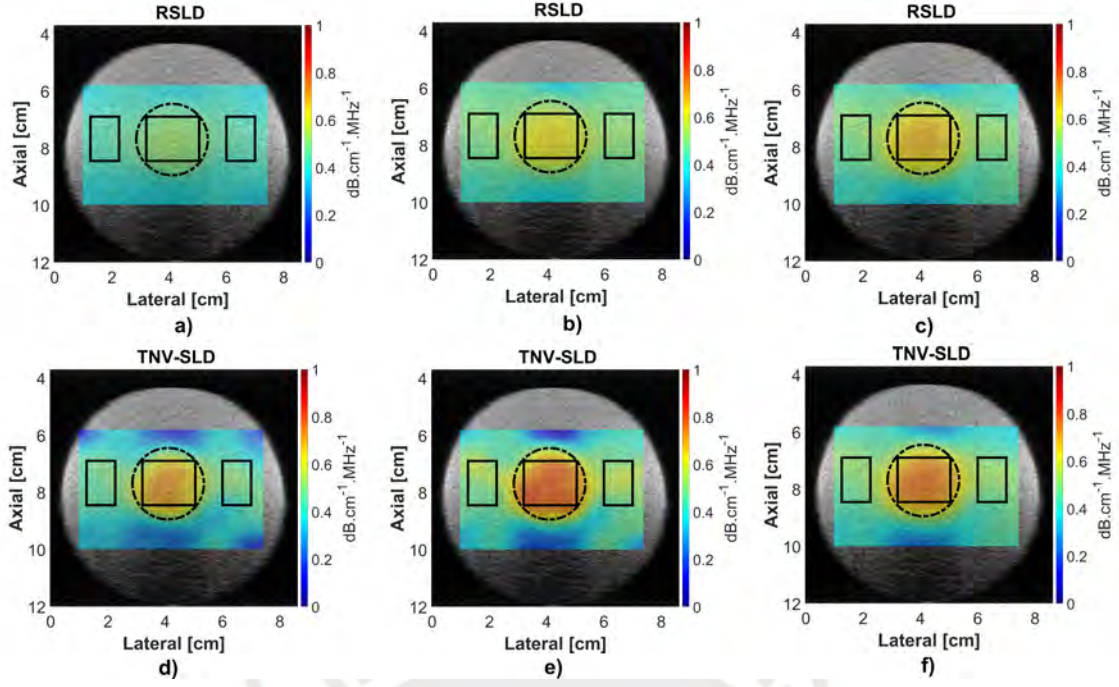


Figure 2.4: ACS maps when using the (a)-(e) RSLD and (f)-(j) TNV-SLD techniques for data block sizes of  $10\lambda \times 10\lambda$ ,  $20\lambda \times 20\lambda$ ,  $30\lambda \times 30\lambda$  for the tissue-mimicking phantom. The black lines outline the regions for calculation metrics.

Table 2.2: MPE, CV and CNR of the final ACS maps with RSLD and TNV-SLD for the tissue-mimicking phantom at different block sizes. Ground-truth values  $1.04 \text{ dB}\cdot\text{cm}^{-1}\cdot\text{MHz}^{-1}$  (inclusion) and  $0.54 \text{ dB}\cdot\text{cm}^{-1}\cdot\text{MHz}^{-1}$  (background).

Block Size	Technique	$\mu$	Inclusion		Background		CNR
			MPE	CV	MPE	CV	
$10\lambda$	RSLD [20]	$10^{4.5}$	46.03	2.63	8.26	2.27	3.59
	TNV-SLD	$10^{4.5}$	<b>28.93</b>	5.99	<b>1.88</b>	5.58	3.95
$20\lambda$	RSLD [20]	$10^{4.5}$	37.68	2.80	1.94	3.06	4.05
	TNV-SLD	$10^{5.5}$	<b>22.51</b>	7.39	<b>1.79</b>	13.39	4.33
$30\lambda$	RSLD [20]	$10^{4.5}$	33.04	3.18	2.72	4.03	4.80
	TNV-SLD	$10^{4.5}$	<b>26.27</b>	4.33	<b>1.89</b>	4.94	5.01
$40\lambda$	RSLD [20]	$10^{4.5}$	32.05	2.81	0.60	3.76	5.10
	TNV-SLD	$10^4$	<b>23.67</b>	3.76	<b>0.36</b>	5.77	5.22
$50\lambda$	RSLD [20]	$10^{4.5}$	27.43	3.15	2.69	4.43	5.11
	TNV-SLD	$10^{5.5}$	<b>22.97</b>	3.77	3.07	5.75	4.99

Outcomes from the tissue-mimicking phantom further validate TNV-SLD's comparative efficacy over RSLD, which produced degraded ACS maps. The metrics, particularly MPE and CNR, quantitatively demonstrate TNV-SLD's advantage in image quality at smaller block sizes.

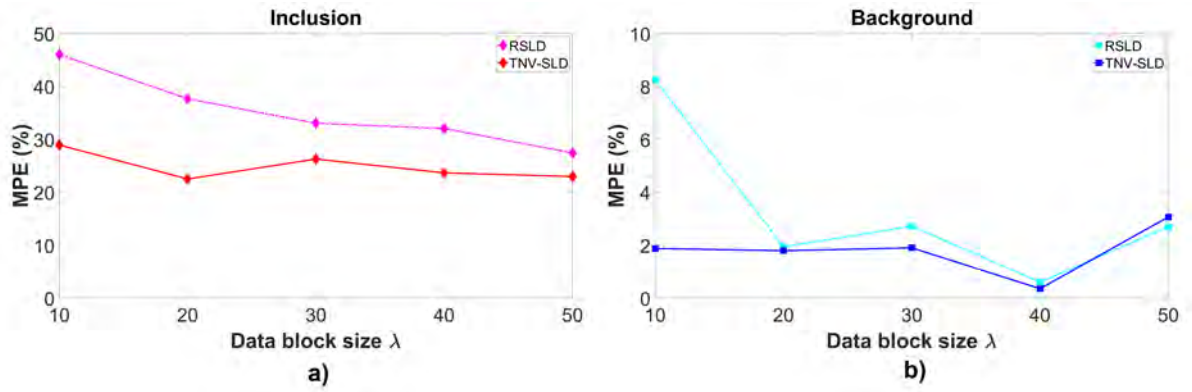


Figure 2.5: MPE at different block sizes in the (a) inclusion and (b) background regions for the tissue-mimicking phantom.

### Impact of the regularization parameter

In order to compare the robustness of both methods, the metrics were calculated for different values of the regularization parameter  $\mu$  as powers of 10. The impact of the  $\mu$  value was evaluated in terms of MPE and CNR, in particular case using a fixed data block size of  $20\lambda \times 20\lambda$  is presented in Fig. 2.6. Similar to the simulation results, the evaluation of the regularization parameter's impact on tissue-mimicking phantom reinforces the TNV-SLD's adaptability and robustness with a wider  $\mu$  value range.

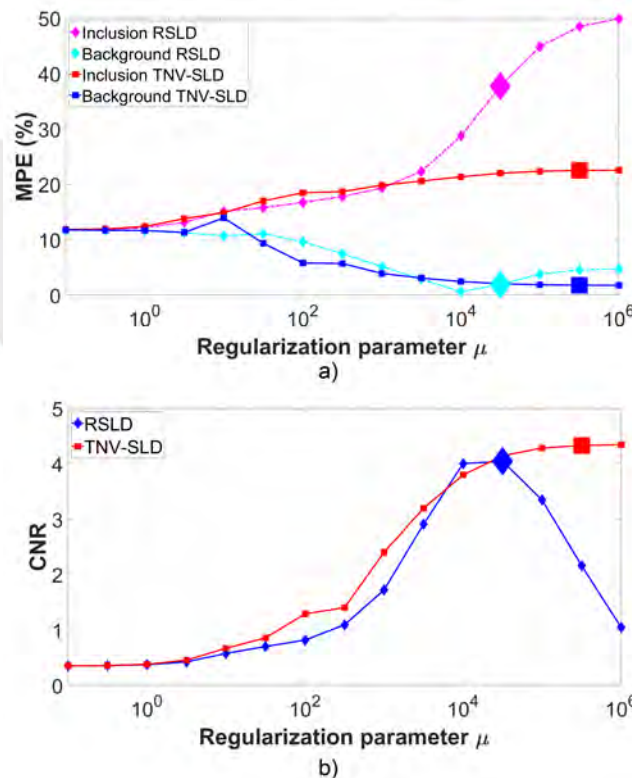


Figure 2.6: (a) MPE, (b) CNR of the ACS for the simulated phantom with the RSLD and TNV-SLD methods, cases with maximum CNR are marked.

## 2.7 Discussion

This chapter compares a new regularization technique labeled TNV-SLD based on the nuclear norm to RSLD in a simulated and tissue-mimicking phantom.

In the inhomogeneous simulation, TNV-SLD reconstructed high-quality ACS maps with a more visible inclusion compared to RSLD (see Fig. 2.1). Both techniques showed low variability in the estimations measured by a similar CV in all block sizes. Nevertheless, TNV-SLD yielded a comparable maximum CNR value with a generally lower error in the inclusion (MPE < 20%) and the background (MPE < 5%) for small block sizes (i.e.  $10\lambda$  and  $20\lambda$ ) in comparison to RSLD (see Fig. 2.2). Therefore, exploiting structure similarities between the ACS and the backscatter term with the TNV prior enhanced the quality of the images and the accuracy of the estimations in terms of bias. Moreover, the CNR enhancement was validated at different values of the regularization parameter  $\mu$ . TNV-SLD showed to be more robust maintaining a relatively stable MPE for the inclusion and background and a higher CNR in a larger range ( $10^2 < \mu < 10^5$ ) in comparison to RSLD (see Fig. 2.3).

Findings from the tissue-mimicking phantoms were in line with the simulation results. TNV-SLD can generate ACS maps without compromising image perception. In Fig. 2.4, it can be seen that RSLD over-regularized and degraded the ACS map, and rendering it difficult to differentiate between the background and inclusion. TNV-SLD managed to maintain a lower bias in the inclusion (MPE < 30%) and the background (MPE < 2%), even with small block sizes (i.e.  $10\lambda$  and  $20\lambda$ ) compared to RSLD (see Fig. 2.5). Therefore, TNV-SLD proved to extend further the spatial resolution of the SLD technique. Additionally, TNV-SLD exhibits less sensitivity to the  $\mu$  parameter, demonstrating a broader range of values ( $10^3 < \mu < 10^6$ ) to maintain a superior CNR with no great impact in the ACS bias (see Fig. 2.6). Future research should focus on incorporating advanced deep unfolding techniques to provide additional spatial support

# Chapter 3

## Multi-frequency joint reconstruction for SLD

This chapter aims to explain the denoising strategy of each spectral ratio developed by Rouyer et al. [24] for the SLD framework. Furthermore, the text will introduce the basics of innovative joint spectral log difference methods that leverage Total Frobenius and Total Nuclear Variation for the denoising of all the spectral ratios.

### 3.1 Total Variation denoising (TV)

The TVSLD technique [24] was proposed to reduce the variability of the ACS estimations. First, the spectral ratios across frequencies  $Y$  are unfolded in the spatial dimensions in vectors, resulting in one vector per frequency.

$$\mathbf{y}_1 = \begin{bmatrix} Y_{1,1,1} \\ Y_{1,2,1} \\ \vdots \\ Y_{1,n,1} \\ Y_{2,1,1} \\ Y_{2,2,1} \\ \vdots \\ Y_{m,n,1} \end{bmatrix}_{mn \times 1}, \mathbf{y}_2 = \begin{bmatrix} Y_{1,1,2} \\ Y_{1,2,2} \\ \vdots \\ Y_{1,n,2} \\ Y_{2,1,2} \\ Y_{2,2,2} \\ \vdots \\ Y_{m,n,2} \end{bmatrix}_{mn \times 1}, \dots, \mathbf{y}_p = \begin{bmatrix} Y_{1,1,p} \\ Y_{1,2,p} \\ \vdots \\ Y_{1,n,p} \\ Y_{2,1,p} \\ Y_{2,2,p} \\ \vdots \\ Y_{m,n,p} \end{bmatrix}_{mn \times 1}. \quad (3.1)$$

TVSLD introduced a spatial regularization denoising strategy of each spectral ratio  $\mathbf{y}_k \in \mathbb{R}^{mn \times 1}$  at frequency  $f_k$ , minimizing the cost functions

$$\arg \min_{\mathbf{u}_k} \frac{1}{2} \|\mathbf{y}_k - \mathbf{u}_k\|_2^2 + \mu \mathcal{R}(\mathbf{u}_k), \quad (3.2)$$

where  $\mathbf{u}_k$  corresponds to the denoised spectral ratio and  $\mu$  is the regularization parameter that controls the trade-off between data fidelity and smoothness.  $\mathcal{R}(\mathbf{u}_k)$  was the single-channel TV regularizer and the minimization of Eq. (3.2) was achieved using the Iteratively Reweighted Least Squares algorithm [48] with a penalization weight  $\psi_k$  which was determined and scaled based on the SNR of the original noisy spectral ratio  $\mathbf{y}_k$ , defined as follows

$$\mathcal{R}(\mathbf{u}_k) = \text{TV}_\psi(\mathbf{u}_k) = \psi_k \text{TV}(\mathbf{u}_k), \quad (3.3)$$

$$\psi_k = \frac{\text{E}[\mathbf{y}_k]}{\sqrt{\text{Var}[\mathbf{y}_k]}}, \quad (3.4)$$

where  $\text{E}[\cdot]$  represents the expected or mean value and  $\text{Var}[\cdot]$  is the variance.

## 3.2 Joint Spectral Log Difference

This method involves jointly denoising all the spectral ratios simultaneously, grouped into a vector denoted by  $\mathbf{y} = [\mathbf{y}_1^T \mathbf{y}_2^T \cdots \mathbf{y}_p^T]^T \in \mathbb{R}^{mnp \times 1}$  among  $p$  frequency channels. Therefore, a new cost function is written as follows

$$\arg \min_{\mathbf{u}} \frac{1}{2} \|\mathbf{y} - \mathbf{u}\|_2^2 + \mu \mathcal{R}(\mathbf{u}) \text{ with} \quad (3.5)$$

$$\mathcal{R}(\mathbf{u}) = \text{TFV}_\psi(\mathbf{u}) \text{ or} \quad (3.6)$$

$$\mathcal{R}(\mathbf{u}) = \text{TNV}_\psi(\mathbf{u}), \quad (3.7)$$

where  $\mathbf{u}$  groups all the denoised spectral ratios. Thus,  $\mathbf{u}$  is considered as a multi-channel 2D image with  $p$  spectral channels  $\mathbf{u} = [\mathbf{u}_1^T \mathbf{u}_2^T \cdots \mathbf{u}_p^T]^T$  and its gradients can be arranged in the Jacobian  $\mathcal{J}(\mathbf{u})$  [34, 35, 45]

$$\mathcal{J}(\mathbf{u}) = \begin{bmatrix} \nabla_x(\mathbf{u}_1) & \nabla_x(\mathbf{u}_2) & \cdots & \nabla_x(\mathbf{u}_p) \\ \nabla_z(\mathbf{u}_1) & \nabla_z(\mathbf{u}_2) & \cdots & \nabla_z(\mathbf{u}_p) \end{bmatrix}^T, \quad (3.8)$$

where  $\nabla_x$  and  $\nabla_z$  denote the gradients in the lateral and axial directions, respectively. The regularization term  $\mathcal{R}(\mathbf{u})$  can be replaced with the Frobenius and nuclear norm of the Jacobian, known as the TFV and TNV, respectively. Both regularizers can couple the frequency channels, and following the strategy of weighting outlined in Eq.(3.4), a penalty term  $\psi_k$  is assigned to each channel.

### 3.2.1 Total Frobenius Variation denoising (TFV)

The Frobenius norm provides a first attempt of edge coupling among the channels and is shown to have a good performance and a favorite selection for a vectorial TV [49]. The TFV can be defined using the mixed  $\ell_{1,F}$ -norm as follows

$$\text{TFV}(\mathbf{u}) = \|\mathcal{J}(\mathbf{u})\|_{1,F} = \sum_{i,j}^{m,n} \|\mathcal{J}(\mathbf{u})\|_F, \quad (3.9)$$

where the Frobenius norm  $\|\cdot\|_F$  of a generic matrix  $Z$  is the square root of the sum of the squares of its elements, given by  $\|Z\|_F = \sqrt{\sum_r |z_r|^2}$ . Furthermore, the weights  $\psi_k$  were applied considering the weighted Frobenius norm [50] as follows

$$\text{TFV}_\psi(\mathbf{u}) = \sum_{i,j}^{m,n} \sqrt{\sum_k^p (\psi_k \nabla_x(\mathbf{u}_k))^2 + (\psi_k \nabla_z(\mathbf{u}_k))^2}. \quad (3.10)$$

### 3.2.2 Total Nuclear Variation denoising (TNV)

The TNV approach uses the nuclear norm of the Jacobian enforcing shared edges and gradient vectors among multi-channel images, being insensitive to contrast or scale differences [35]. TNV is based on geometrical structure constraints among channels and is defined using the mixed  $\ell_{1,*}$ -norm

$$\text{TNV}(\mathbf{u}) = \|\mathcal{J}(\mathbf{u})\|_{1,*} = \sum_{i,j}^{m,n} \|\mathcal{J}(\mathbf{u})\|_*, \quad (3.11)$$

where the nuclear norm  $\|\cdot\|_*$  of a generic matrix  $Z$  is the sum of its singular values  $\sigma$ , given by  $\|Z\|_* = \sum_r \sigma_r(Z)$ . Moreover, the weights  $\psi_k$  were applied considering the weighted nuclear norm [51] as follows

$$\text{TNV}_\psi(\mathbf{u}) = \sum_{i,j}^{m,n} \sum_k^p \psi_k \sigma_k(\mathcal{J}(\mathbf{u})). \quad (3.12)$$

### 3.2.3 Algorithmic implementation

First, TNV and TFV can be defined using the notation of dual-norm [34], using an auxiliary variable  $z$

$$\text{TFV}_\psi(\mathbf{u}) = \max_z \langle \mathcal{J}(\mathbf{u}), z \rangle - \delta_{\mathcal{F}}(z), \quad (3.13)$$

$$\text{TNV}_\psi(\mathbf{u}) = \max_z \langle \mathcal{J}(\mathbf{u}), z \rangle - \delta_{\mathcal{N}}(z), \quad (3.14)$$

where  $\langle \cdot, \cdot \rangle$  is the inner product,  $\delta(z)$  is the well-known indicator function, and  $\mathcal{N}$  and  $\mathcal{F}$  are the sets defined by  $\mathcal{F} = \{z : \|z\|_F \leq 1\}$  and  $\mathcal{N} = \{z : \sigma_{max} \leq 1\}$ .

Hence, the cost function in Eq. (3.5) can be formulated as a saddlepoint problem, which involves both minimization and maximization optimization problems

$$\arg \min_{\mathbf{u}} \max_z \frac{1}{2} \|\mathbf{y} - \mathbf{u}\|_2^2 - \mu \delta_{\mathcal{K}}(z) + \mu \langle \mathcal{J}(\mathbf{u}), z \rangle, \quad (3.15)$$

where  $\delta_{\mathcal{K}}$  is a generic indicator function with a set  $\mathcal{K}$  that can be replaced for  $\mathcal{F}$  or  $\mathcal{N}$  for the TFV and TNV, respectively. The solution of Eq. (3.15) can be derived using the Primal-Dual Splitting method with proximal operators [41]. The Algorithm 2 is suitable for a generic problem as follows

$$\arg \min_{\mathbf{u}} f(\mathbf{u}) = \arg \min_{\mathbf{u}} \max_z G(\mathbf{u}) - H^*(z) + \langle L(\mathbf{u}), z \rangle \quad (3.16)$$

The first operator  $\text{prox}_{\tau G}$  corresponds to the  $\ell_2$ -norm data fidelity term, which measures the discrepancy between the observed data and the reconstructed data by the Euclidean distance. For this case, since it is a denoising approach, the proximal operator is expressed as

$$\text{prox}_{\tau G}(x) = \frac{x + \tau \mathbf{y}}{1 + \tau}. \quad (3.17)$$

The second operator  $\text{prox}_{\sigma H^*}$  can be derived Moreau's identity by  $\text{prox}_{H/\sigma}$ . For the TFV, it corresponds to the projection onto the  $\ell_2$ -norm ball [46]. For the TNV, it consists

---

**Algorithm 2** Primal-Dual Splitting Algorithm

---

$$G(\mathbf{u}) = \frac{1}{2}\|\mathbf{y} - \mathbf{u}\|_2^2, \quad H^*(z) = \mu\delta(z), \quad L(\mathbf{u}) = \mathcal{J}(\mathbf{u})$$

**repeat**

$$\hat{\mathbf{u}}_{n+1} := \text{prox}_{\tau G}(\mathbf{u}_n - \tau L^*(z_n))$$

$$\hat{z}_{n+1} := \text{prox}_{\sigma H^*}(z_n + \sigma L(2\hat{\mathbf{u}}_{n+1} - \mathbf{u}_n))$$

$$(\mathbf{u}_{n+1}, z_{n+1}) := \rho(\hat{\mathbf{u}}_{n+1}, \hat{z}_{n+1}) + (1 - \rho)(\mathbf{u}_n, z_n)$$

**until**  $\frac{\|f(\mathbf{u}_{n+1}) - f(\mathbf{u}_n)\|_2}{\|f(\mathbf{u}_n)\|_2} < \epsilon$ ; convergence criteria

---

of a soft-thresholding operation on the weighted singular values ( $\tilde{\sigma}_k = \max(\sigma_k - \mu\psi_k, 0)$ ) [43, 52]. The  $\tau, \sigma$  and  $\rho$  are relaxation and proximal parameters related to the convergence speed of the algorithm. The impact of their value has been studied extensively in [46], suggesting practical criteria of  $\sigma = (\rho - 0.5\tau)/8\tau$ ,  $\rho \approx 1.99$ . Lastly,  $\tau$  can be achieved by grid search inspection, for this case  $\tau = 0.001$  was considered.

### 3.3 Dataset

#### 3.3.1 Simulated data

A simulated phantom was created using the k-Wave toolbox in MATLAB [47]. The simulation consisted of a circular inclusion with a 10 mm radius embedded in a homogeneous background at 25 mm depth. A 128-element array transducer with a 0.3 mm pitch and 6.66 MHz central frequency was used to generate the ultrasound data. The background and inclusion were assigned to have ACS values of  $0.5 \text{ dB}\cdot\text{cm}^{-1}\cdot\text{MHz}^{-1}$  and  $1 \text{ dB}\cdot\text{cm}^{-1}\cdot\text{MHz}^{-1}$ , respectively. To compensate for diffraction effects, a simulated homogeneous reference phantom with an ACS of  $0.4 \text{ dB}\cdot\text{cm}^{-1}\cdot\text{MHz}^{-1}$  was employed.

#### 3.3.2 Experimental phantom

An agar-based tissue-mimicking phantom was used (Model 049, manufactured by CIRS, VA, USA). The phantom had a spherical inclusion with a 10 mm radius within a homogeneous background. The ground truth ACS values were reported by the manufacturer to be  $0.97 \text{ dB}\cdot\text{cm}^{-1}\cdot\text{MHz}^{-1}$  for the inclusion and  $0.55 \text{ dB}\cdot\text{cm}^{-1}\cdot\text{MHz}^{-1}$  for the background. Data was acquired using a SonixTouch ultrasound scanner (Analogic Ultrasound, Peabody, MA, USA) with an L14-5 linear transducer. Analysis of the spectrum of the RF data identified a peak frequency of 4.1 MHz. For diffraction compensation, a homogeneous reference phantom from the same manufacturer was used with a reported ACS of  $0.53 \text{ dB}\cdot\text{cm}^{-1}\cdot\text{MHz}^{-1}$ .

#### 3.3.3 *Ex vivo* tissue

Data from a physical phantom described in [53] was used. The phantom was prepared using agar (Sigma-Aldrich, St. Louis, MO) and graphite powder (John Deere, Moline, IL) with an embedded *ex vivo* fatty porcine tissue from a pork belly. The ACS in the background was estimated with insertion loss techniques, reporting to be  $0.65 \text{ dB}\cdot\text{cm}^{-1}\cdot\text{MHz}^{-1}$ . For this case, a homogeneous phantom with background-like characteristics served as a

reference for diffraction compensation. The RF acquisition was performed with a Vantage 256 system (Verasonics Inc., Kirkland, WA) and an L9-4/38 transducer (BK Ultrasound, Peabody, MA). RF data frames were acquired using a plane wave technique without incorporating angular compounding.

### 3.4 Reconstruction and evaluation of the ACS

The ACS maps were generated using block sizes of  $20\lambda \times 20\lambda$  (where  $\lambda$  represents the wavelength). The bandwidth was selected based on the 20 dB decay range, resulting in 3 – 9 MHz for the simulated and experimental phantoms, 3.5 – 8.5 MHz for the *ex vivo* sample and 4 – 11 MHz for the *in vivo* samples. The axial and lateral overlap of the blocks was fixed at 80%. The ACS maps were obtained by applying a linear fit to the denoised spectral ratios  $\mathbf{u}$  using the TV, TFV TNV approaches (as shown in Fig.3.1). Different values of the regularization parameter  $\mu$  were computed in a logarithmic range from  $10^{-1} - 10^1$ . For this study, the optimal  $\mu$  value was determined by minimizing the Mean Percentage Error (MPE) of the ACS for each method.

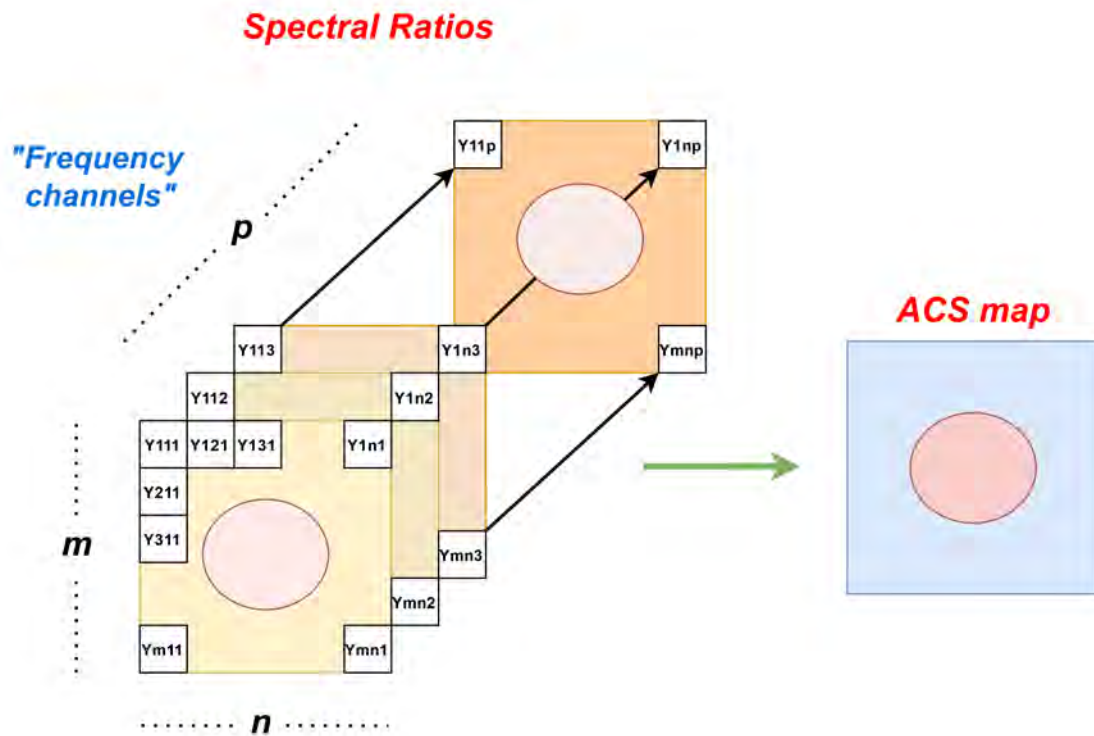


Figure 3.1: Workflow showing the reconstruction of the ACS maps from the denoised spectral ratios.



## 3.5 Results

### 3.5.1 Simulated phantom

ACS maps were estimated for the heterogeneous simulated phantom using the TV ( $\mu = 10^{0.6}$ ) method and the proposed joint reconstruction strategies TNV ( $\mu = 10^{0.6}$ ) and TFV ( $\mu = 10^{0.65}$ ) in Fig. 3.2). Metrics such as mean, standard deviation, MPE, SDPE and CNR for all the block sizes are synthesized in Table 3.1, and the obtained CNR for the inclusion and background at different block sizes are displayed in Fig. 3.3. The TNV method demonstrated superior accuracy and consistency, particularly notable in CNR values, thereby establishing its effectiveness over TV and TFV. This comparison underscores TNV's potential for enhanced image quality and precision in simulated environments.

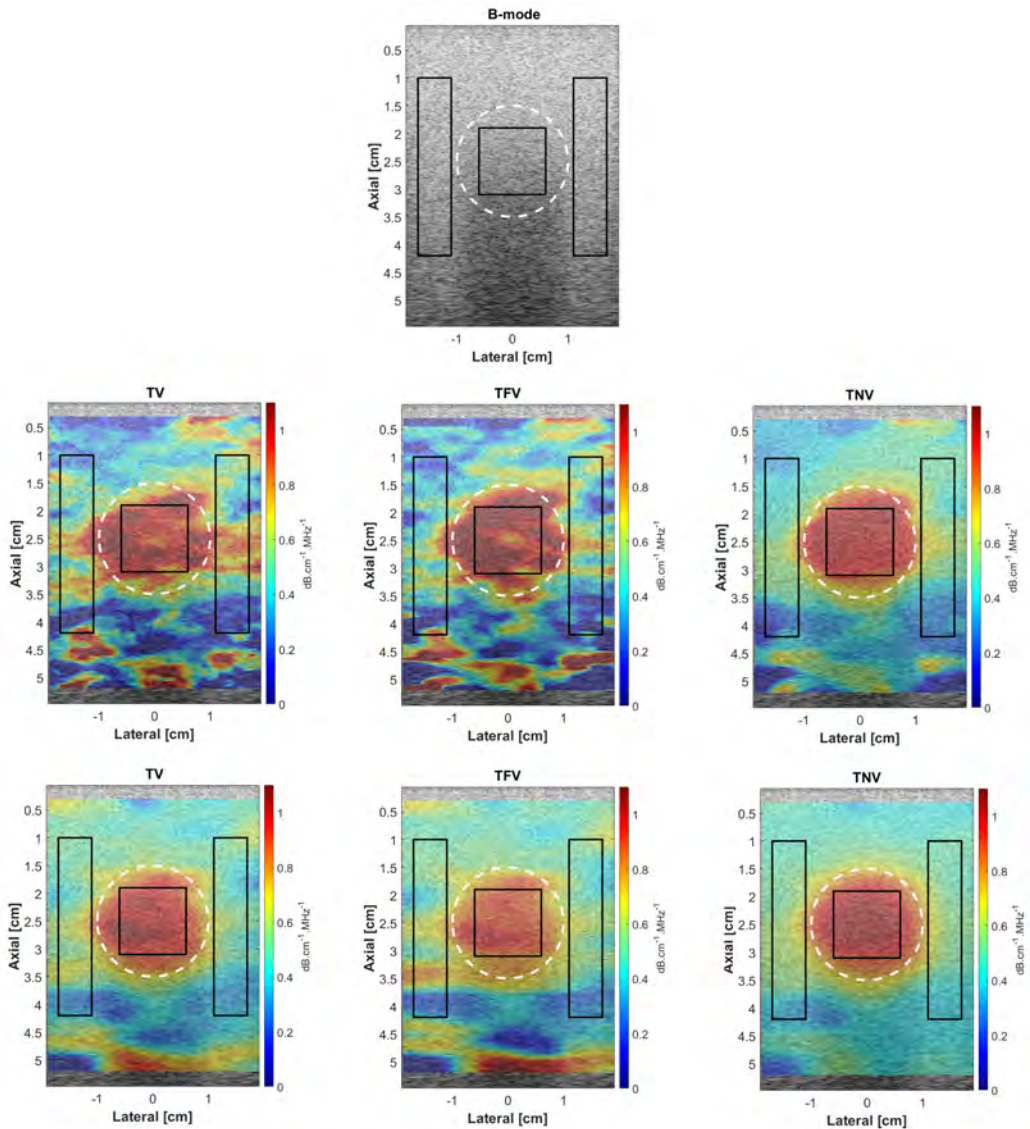


Figure 3.2: ACS maps generated for the simulated phantom when using (b-e) TV, (c-f) TFV and (d-g) TNV techniques, respectively. The lines outline the regions for metrics

Table 3.1: Comparison of mean, std, MPE, SDPE and CNR for the ACS maps of the simulated phantom using the proposed joint reconstruction techniques (TFV and TNV) and TV. Ground-truth values  $1 \text{ dB}\cdot\text{cm}^{-1}\cdot\text{MHz}^{-1}$  (inclusion) and  $0.5 \text{ dB}\cdot\text{cm}^{-1}\cdot\text{MHz}^{-1}$  (background).

Block Size	Metric	TV ( $\mu = 10^{0.6}$ )		TFV ( $\mu = 10^{0.65}$ )		TNV ( $\mu = 10^{0.6}$ )	
		Inclusion	Background	Inclusion	Background	Inclusion	Background
$10\lambda$	$\bar{x} \pm \sigma$	$1.08 \pm 0.06$	$0.50 \pm 0.18$	$1.08 \pm 0.15$	$0.42 \pm 0.24$	$1.00 \pm 0.04$	$0.47 \pm 0.13$
	MPE (%)	7.7	0.9	8.2	16.6	0.2	7.0
	SDPE (%)	6.5	36.0	14.8	48.3	3.6	26.8
	CNR	2.9		2.3		3.7	
$20\lambda$	$\bar{x} \pm \sigma$	$0.99 \pm 0.05$	$0.49 \pm 0.11$	$0.91 \pm 0.05$	$0.51 \pm 0.14$	$1.01 \pm 0.04$	$0.53 \pm 0.09$
	MPE (%)	1.5	1.2	8.7	2.0	1.3	5.2
	SDPE (%)	5.1	22.1	4.7	27.6	3.6	17.7
	CNR	3.9		2.7		4.9	
$30\lambda$	$\bar{x} \pm \sigma$	$0.95 \pm 0.04$	$0.50 \pm 0.11$	$0.93 \pm 0.02$	$0.54 \pm 0.10$	$0.99 \pm 0.03$	$0.54 \pm 0.10$
	MPE (%)	4.8	0.2	6.6	7.6	1.0	8.5
	SDPE (%)	4.2	21.9	1.6	20.9	3.0	19.5
	CNR	3.7		3.6		4.2	
$40\lambda$	$\bar{x} \pm \sigma$	$0.95 \pm 0.05$	$0.54 \pm 0.10$	$0.97 \pm 0.04$	$0.55 \pm 0.10$	$1.02 \pm 0.04$	$0.55 \pm 0.10$
	MPE (%)	5.0	9.0	3.5	10.3	1.6	10.1
	SDPE (%)	5.4	20.8	3.5	19.9	3.9	20.0
	CNR	3.3		3.7		4.1	
$50\lambda$	$\bar{x} \pm \sigma$	$0.92 \pm 0.06$	$0.57 \pm 0.09$	$0.92 \pm 0.04$	$0.56 \pm 0.09$	$0.90 \pm 0.04$	$0.56 \pm 0.08$
	MPE (%)	8.1	14.1	7.9	11.3	10.2	12.1
	SDPE (%)	6.1	17.3	3.8	18.6	3.5	16.9
	CNR	3.1		3.5		3.5	

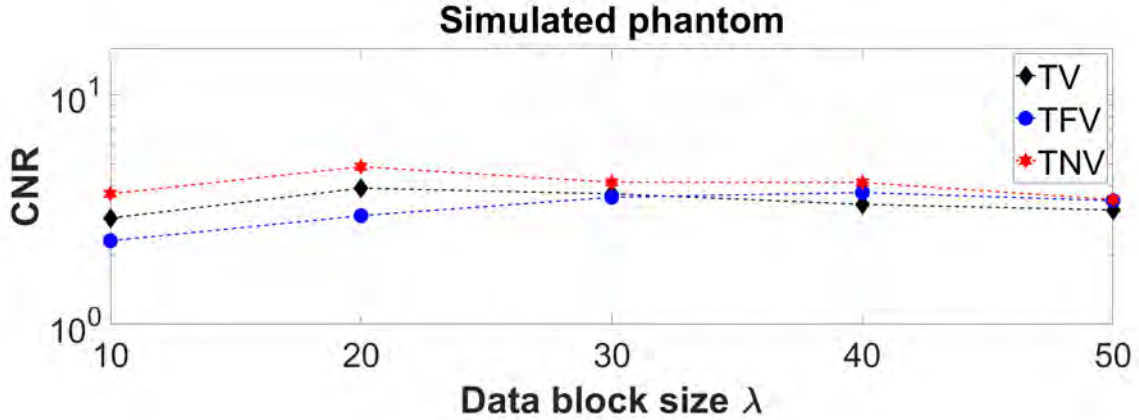


Figure 3.3: CNR of the ACS maps using the TV, TFV and TNV techniques at different block sizes for the simulated phantom.

### 3.5.2 Experimental phantom

The generated ACS maps of the experimental phantom with TV ( $\mu = 10^{0.65}$ ), TFV ( $\mu = 10^{0.7}$ ) and TNV ( $\mu = 10^{0.65}$ ) techniques are shown in Fig. 3.4. Table 3.2 details the mean, standard deviation, MPE, SDPE and CNR for all the block sizes, and the obtained CNR for the inclusion and background at different block sizes are displayed in Fig. 3.5.

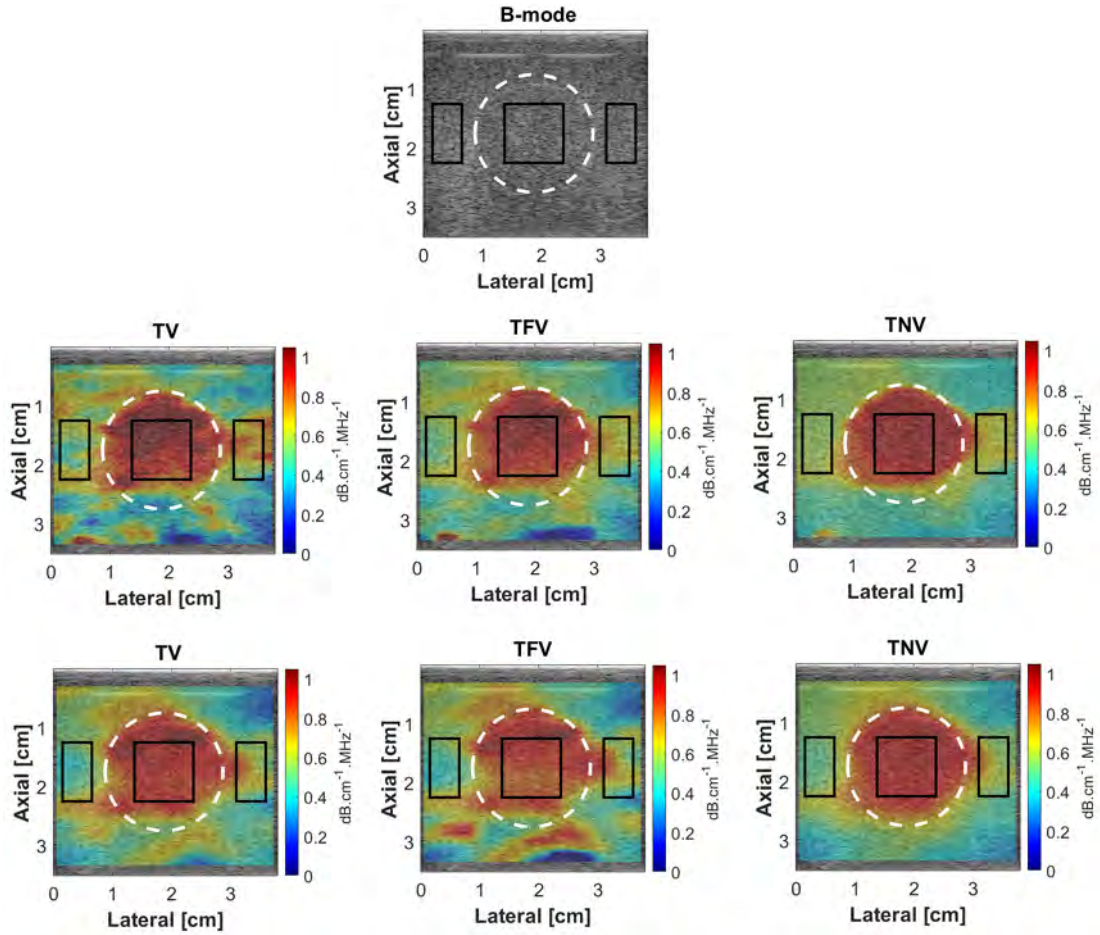


Figure 3.4: ACS maps generated for the experimental phantom when using (b-e) TV, (c-f) TFV, and (d-g) TNV techniques, respectively. The lines outline the regions for metrics.

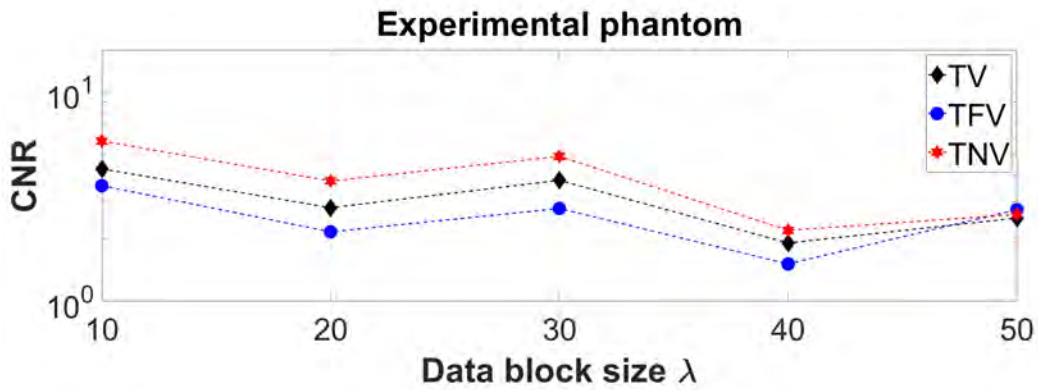


Figure 3.5: CNR of the ACS maps using the TV, TFV and TNV techniques at different block sizes for the experimental phantom.

Results show TNV's advantage in achieving higher quality images with low MPE compared to TV and TFV, emphasizing its robustness and reliability.

Table 3.2: Comparison of mean, std, MPE, SDPE and CNR for the ACS maps of the experimental phantom using the proposed joint reconstruction techniques (TFV and TNV) and TV. Ground-truth values  $0.97 \text{ dB}\cdot\text{cm}^{-1}\cdot\text{MHz}^{-1}$  (inclusion) and  $0.55 \text{ dB}\cdot\text{cm}^{-1}\cdot\text{MHz}^{-1}$  (background).

Block Size	Metric	TV ( $\mu = 10^{0.65}$ )		TFV ( $\mu = 10^{0.7}$ )		TNV ( $\mu = 10^{0.65}$ )	
		Inclusion	Background	Inclusion	Background	Inclusion	Background
10 $\lambda$	$\bar{x} \pm \sigma$	$1.06 \pm 0.07$	$0.64 \pm 0.07$	$0.96 \pm 0.06$	$0.61 \pm 0.07$	$0.97 \pm 0.03$	$0.62 \pm 0.05$
	MPE (%)	9.1	15.7	1.1	10.1	0.2	11.9
	SDPE (%)	6.8	11.9	6.4	12.9	2.7	9.0
	CNR	4.3		3.6		5.8	
20 $\lambda$	$\bar{x} \pm \sigma$	$0.93 \pm 0.04$	$0.58 \pm 0.11$	$0.87 \pm 0.05$	$0.57 \pm 0.12$	$0.99 \pm 0.03$	$0.58 \pm 0.10$
	MPE (%)	4.6	5.5	10.3	4.0	1.7	4.8
	SDPE (%)	3.7	20.4	5.2	22.5	2.6	18.3
	CNR	2.8		2.1		3.8	
30 $\lambda$	$\bar{x} \pm \sigma$	$0.94 \pm 0.03$	$0.60 \pm 0.08$	$0.89 \pm 0.07$	$0.59 \pm 0.11$	$0.94 \pm 0.01$	$0.64 \pm 0.05$
	MPE (%)	3.3	9.2	8.1	7.5	3.3	17.0
	SDPE (%)	3.5	14.0	6.9	19.6	1.1	9.8
	CNR	3.8		2.3		4.9	
40 $\lambda$	$\bar{x} \pm \sigma$	$0.88 \pm 0.06$	$0.61 \pm 0.13$	$0.86 \pm 0.08$	$0.60 \pm 0.15$	$0.90 \pm 0.03$	$0.64 \pm 0.11$
	MPE (%)	8.9	10.7	11.4	9.1	7.2	15.6
	SDPE (%)	5.7	23.3	7.9	26.9	3.0	20.4
	CNR	1.9		1.5		2.2	
50 $\lambda$	$\bar{x} \pm \sigma$	$0.87 \pm 0.04$	$0.61 \pm 0.09$	$0.86 \pm 0.03$	$0.62 \pm 0.08$	$0.85 \pm 0.03$	$0.62 \pm 0.08$
	MPE (%)	10.0	11.6	11.1	12.1	12.0	12.5
	SDPE (%)	3.8	15.5	3.1	14.4	3.4	14.3
	CNR	2.5		2.7		2.6	

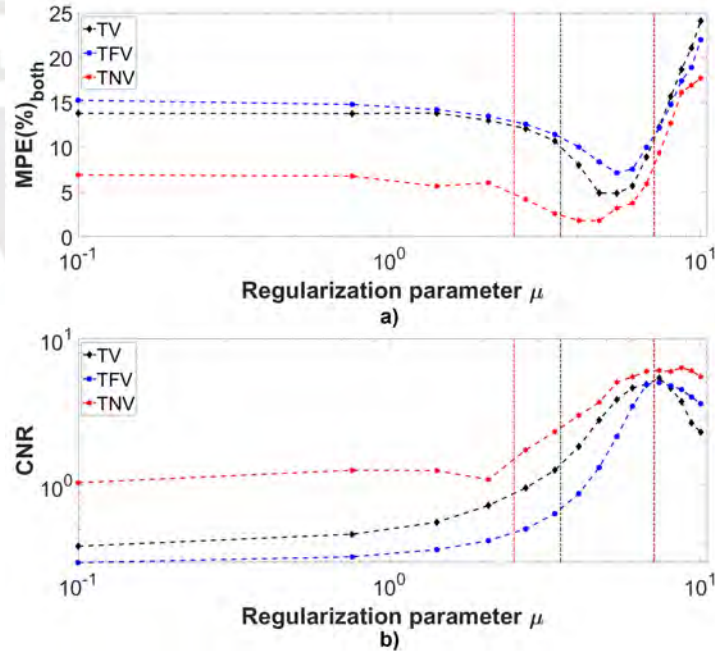


Figure 3.6: (a) Average MPE of both regions, (b) CNR of the experimental phantom with the TV, TFV and TNV methods for a data block size of  $20\lambda$ . The optimal range of  $\mu$  is identified by minimizing the MPE denoted by the vertical dashed lines.

Table 3.3: Comparison of mean, std and CNR for the ACS maps of the *ex vivo* porcine tissue using the proposed joint reconstruction techniques (TFV and TNV) and TV

Block Size	Metric	TV ( $\mu = 10^{0.65}$ )		TFV ( $\mu = 10^{0.7}$ )		TNV ( $\mu = 10^{0.65}$ )	
		Inclusion	Background	Inclusion	Background	Inclusion	Background
10 $\lambda$	$\bar{x} \pm \sigma$	1.41 $\pm$ 0.20	0.62 $\pm$ 0.11	1.37 $\pm$ 0.24	0.64 $\pm$ 0.12	1.39 $\pm$ 0.15	0.65 $\pm$ 0.11
	CNR	3.3		2.7		3.9	
20 $\lambda$	$\bar{x} \pm \sigma$	1.42 $\pm$ 0.14	0.70 $\pm$ 0.06	1.65 $\pm$ 0.29	0.51 $\pm$ 0.13	1.56 $\pm$ 0.13	0.64 $\pm$ 0.10
	CNR	4.6		3.5		5.4	
30 $\lambda$	$\bar{x} \pm \sigma$	1.52 $\pm$ 0.17	0.58 $\pm$ 0.12	1.48 $\pm$ 0.21	0.63 $\pm$ 0.08	1.49 $\pm$ 0.13	0.60 $\pm$ 0.12
	CNR	4.4		3.8		4.9	

### 3.5.3 Ex Vivo Tissue

The generated ACS maps for the *ex vivo* porcine tissue with TV ( $\mu = 10^{0.65}$ ), TFV ( $\mu = 10^{0.7}$ ) and TNV ( $\mu = 10^{0.65}$ ) techniques are shown in Fig 3.7. Table 3.3 presents the mean, standard deviation and CNR. Fig. 3.8 displays the obtained CNR at different block sizes. The MPE was not calculated for this case, since the ground-truth value of the tissue was not available. Outcomes demonstrate TNV’s ability to closely match literature values, showcasing its applicability and accuracy in biological samples, and yielding superior CNR values.

## 3.6 Discussion

In this chapter, joint reconstruction techniques based on the Frobenius (TFV) and nuclear norm (TNV) have been evaluated in simulated and experimental phantoms and *ex vivo* porcine tissue.

In the simulated phantom, the TV approach limitations can be observed, particularly in the block size. By using small block sizes (10 $\lambda$  and 20 $\lambda$ ), TV reached higher variability (SDPE > 5%). The TFV approach achieved no noticeable enhanced results compared to TV, while TNV obtained more accurate (MPE < 4%) and higher-quality ACS maps with a CNR > 3.5 (see Fig. 3.3). Moreover, TNV reconstructed ACS maps with cleaner edges between inclusion and background (see Fig. 3.2).

The results from the experimental phantoms exhibited a similar tendency to the simulation. TNV estimated ACS with generally lower variability for the inclusion (SDPE < 3.5%) and background (SDPE < 20%). The TFV method failed to generate enhanced ACS images, achieving a slightly below performance to the TV. Nonetheless, the TNV reached a lower bias for 10 $\lambda$  and 20 $\lambda$  block sizes with MPE < 2% (inclusion) and MPE < 12% (background) with the greatest CNR value (see Fig. 3.5), extending the trade-off between spatial resolution and MPE compared to the TV limitation (see Fig. 3.4).

Additional results were generated from an *ex vivo* porcine tissue sample embedded within an agar medium. In a previous work [54], porcine tissue attenuation was characterized by reporting an ACS of around 1.5 dB·cm<sup>-1</sup>·MHz<sup>-1</sup> for subcutaneous fat layers. The results, as presented in Table 3.3, demonstrate that the estimations were in line with the findings reported in the literature. Notably, the best outcomes were obtained when using data block sizes of 20 $\lambda$ . The ACS in the inclusion was estimated to be 1.42  $\pm$  0.14 dB·cm<sup>-1</sup>·MHz<sup>-1</sup> (TV), 1.65  $\pm$  0.29 dB·cm<sup>-1</sup>·MHz<sup>-1</sup> (TFV) and 0.51  $\pm$  0.13 dB·cm<sup>-1</sup>·MHz<sup>-1</sup>

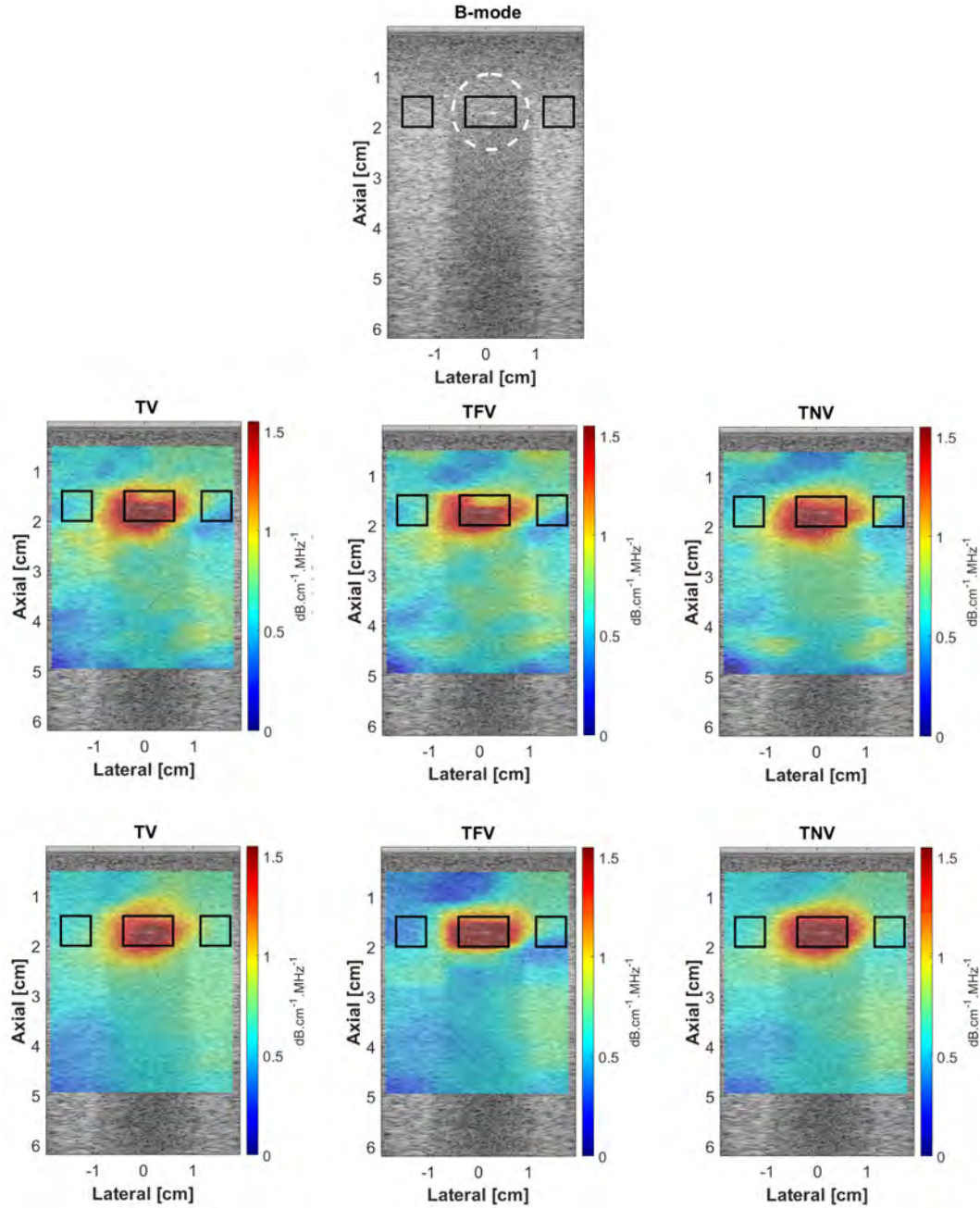


Figure 3.7: ACS maps generated for the *ex vivo* porcine tissue with  $10\lambda$  with and  $20\lambda$  when using (b-e) TV, (c-f) TFV and (d-g) TNV techniques, respectively. The lines outline the regions for metrics.

(TNV). In the case of the background, the ACS was found to be  $0.70 \pm 0.06 \text{ dB}\cdot\text{cm}^{-1}\cdot\text{MHz}^{-1}$  (TV),  $0.51 \pm 0.13 \text{ dB}\cdot\text{cm}^{-1}\cdot\text{MHz}^{-1}$  (TFV) and  $0.64 \pm 0.10 \text{ dB}\cdot\text{cm}^{-1}\cdot\text{MHz}^{-1}$  (TNV). The TNV approach yielded the most favorable results, exhibiting a superior CNR value (see Fig. 3.8). These findings suggest that TNV is suitable beyond numerical and physical phantoms and shows greater potential with smaller block sizes assessing highly accurate estimations with a greater spatial resolution for characterization of potential minuscule

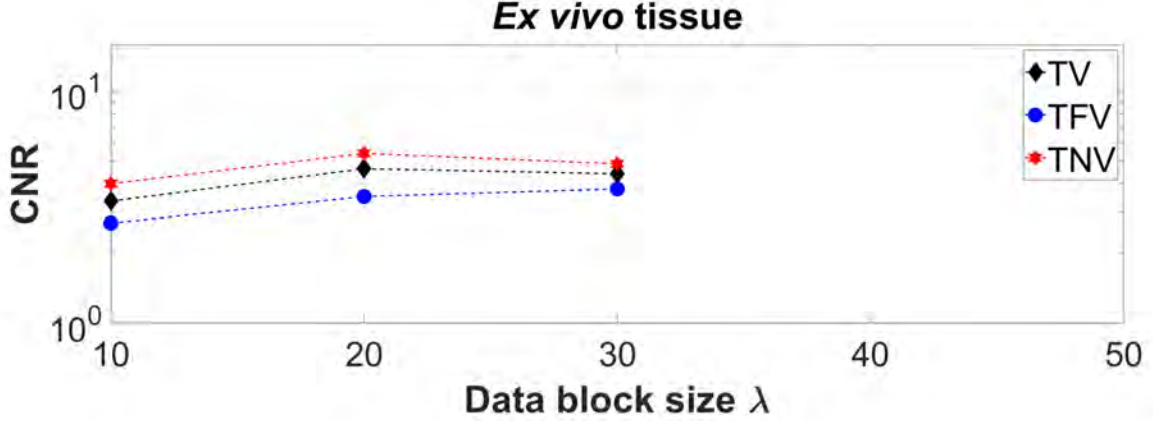


Figure 3.8: CNR of the ACS maps using the TV, TFV and TNV techniques at different block sizes for the *ex vivo* porcine tissue.

regions of interest (see Fig. 3.7).

The impact of the regularization parameter  $\mu$  in the quality of the ACS maps was evaluated for the TV, TFV and TNV techniques in terms of the MPE and CNR for the experimental phantom while using a block size of  $20\lambda$  (see Fig. 3.6). The image quality measured by the CNR remained higher with the TNV method for all the computed  $\mu$  values with a generally lower MPE in comparison to TV and TFV. It is worth mentioning, that large values of the regularization parameter ( $\mu > 10^{0.9}$ ) start to degrade the CNR in all techniques. This was expected since the spectral ratios will be overdenoised merging all regions, making it impossible to distinguish between inclusion and background. Nevertheless, there is a significant range of the regularization parameter for the TV ( $10^{0.55} < \mu < 10^{0.85}$ ), TFV ( $10^{0.55} < \mu < 10^{0.85}$ ) and TNV ( $10^{0.4} < \mu < 10^{0.85}$ ) to assess a low bounded bias (MPE < 12%) in both inclusion and background with a high CNR. Furthermore, the joint techniques were compatible with a fixed weight per spectral ratio according to its level of noise, measured by the SNR. Hence, further research should be conducted to explore the implementation of adaptive and deep unfolded techniques for weight selection.

The main reason for the improved performance of the TNV lies in the nature of the spectral ratios. It was observed that the spectral ratios are highly contaminated with noise and the structures present in the spectral ratios exhibit a low dynamic range, thus the magnitude of the gradients of the channels are expected to be at different scales. It has been extensively reported that the Frobenius norm for a vectorial total variation is sensitive to scale constraints [35, 55]. On the contrary, the nuclear norm promotes gradient alignment and parallelism among the channels, assessing greater reconstructions [34]. Therefore, for the SLD framework, the TNV proves to be a better strategy to exploit common geometrical structures among the frequency channels. Moreover, TNV effectively overcomes a conventional constraint encountered by spectral methods in terms of spatial resolution and quality of the ACS estimations.

# Chapter 4

## Conclusions

In Chapter 2, we have shown the effects of coupling information of the BSC and ACS term directly for the SLD inverse problem. A new regularization joint method based on the total nuclear variation (TNV-SLD) was employed. The spatial support from the backscatter term has enhanced the quality and accuracy of the ACS maps. Results from a simulation and a physical phantom suggest TNV-SLD provides a better trade-off between MPE and CNR compared to RSLD. Furthermore, the TNV-SLD method seems to be more robust than RSLD in terms of the regularization parameter  $\mu$ , surpassing the common RSLD issue of over-regularizing the image and degrading the MPE.

In Chapter 3, a new multi-frequency prior was proposed for joint denoising the spectral ratios. Two modifications to the TV, based on the Frobenius (TFV) and nuclear norm (TNV) were compared for the joint denoising of the spectral ratios across the frequency channels. Results obtained from simulated and experimental phantoms, and *ex vivo* porcine tissue demonstrated that coupling information of the spectral ratios leads to enhanced ACS maps with greater CNR, even with small data block sizes, thereby assessing better spatial resolution.

In summary, the TNV proved to be a suitable approach for coupling information from both the ACS and BSC terms in the regularized joint approach, as well as spectral ratios in the joint denoising approach. The TNV, founded on the nuclear norm, promotes gradient alignment and parallelism across the channels without being sensitive to scale constraints, a limitation often found in other norms. In terms of achieving a lower MPE, higher CNR, and enhanced visual quality of ACS images, TNV demonstrated superior performance compared to both the previous techniques. The enhanced performance of the TNV is consistent with results reported in other imaging modalities, where the TNV reported superior results in multi-channel inverse problems, yielding images of a higher quality.



# Bibliography

- [1] Michael L. Oelze, “Quantitative ultrasound techniques and improvements to diagnostic ultrasonic imaging,” in *2012 IEEE International Ultrasonics Symposium (IUS)*. IEEE, 2012, pp. 232–239.
- [2] Noushin Jafaripisheh, Timothy J. Hall, Hassan Rivaz, and Ivan M. Rosado-Mendez, “Analytic global regularized backscatter quantitative ultrasound,” *IEEE Transactions on Ultrasonics, Ferroelectrics, and Frequency Control*, vol. 68, no. 5, pp. 1605–1617, 2020.
- [3] Kibo Nam, James A Zagzebski, and Timothy J. Hall, “Quantitative assessment of in vivo breast masses using ultrasound attenuation and backscatter,” *Ultrasonic Imaging*, vol. 35, no. 2, pp. 146–161, 2013.
- [4] Julien Rouyer, T. Cueva, A Portal, T. Yamamoto, and RJPP Lavarello, “Attenuation coefficient estimation of the healthy human thyroid in vivo,” *Physics Procedia*, vol. 70, pp. 1139–1143, 2015.
- [5] Daniel Jesper, Daniel Klett, Barbara Schellhaas, Lukas Pfeifer, Moritz Leppkes, Maximilian Waldner, Markus F Neurath, and Deike Strobel, “Ultrasound-based attenuation imaging for the non-invasive quantification of liver fat - a pilot study on feasibility and inter-observer variability,” *IEEE Journal of Translational Engineering in Health and Medicine*, vol. 8, pp. 1–9, 2020.
- [6] Yi-Chun Du, Yung-Fu Chen, Chi-Jeng Lin, Yu-Ching Lin, and Tainsong Chen, “The application of quantitative ultrasound (qus) on study of aging effects of achilles tendons,” in *2005 IEEE Engineering in Medicine and Biology 27th Annual Conference*. IEEE, 2006, pp. 6344–6347.
- [7] Andres Coila, Gabriela Torres, Julien Rouyer, Sara Aristizabal, Matthew Urban, and Roberto Lavarello, “Recent developments in spectral-based ultrasonic tissue characterization,” in *2018 IEEE 15th International Symposium on Biomedical Imaging (ISBI 2018)*. IEEE, 2018, pp. 1018–1021.
- [8] Johan Polack, Andres Coila, Michael Oelze, and Roberto Lavarello, “Analysis of the accuracy and precision of the least square fitting method for simultaneous estimation of backscatter and attenuation coefficients,” in *2018 IEEE International Ultrasonics Symposium (IUS)*. IEEE, 2018, pp. 1–4.

- [9] Guy Cloutier, François Destrempes, François Yu, and An Tang, “Quantitative ultrasound imaging of soft biological tissues: a primer for radiologists and medical physicists,” *Insights into Imaging*, vol. 12, no. 1, pp. 1–20, 2021.
- [10] Iman Rafati, François Destrempes, Ladan Yazdani, Marc Gesnik, An Tang, and Guy Cloutier, “Regularized ultrasound phantom-free local attenuation coefficient slope (acs) imaging in homogeneous and heterogeneous tissues,” *IEEE Transactions on Ultrasonics, Ferroelectrics, and Frequency Control*, vol. 69, no. 12, pp. 3338–3352, 2022.
- [11] Timothy A. Bigelow and William D O'Brien Jr., “Impact of local attenuation approximations when estimating correlation length from backscattered ultrasound echoes,” *The Journal of the Acoustical Society of America*, vol. 120, no. 1, pp. 546–553, 2006.
- [12] M. Fink, F. Hottier, and J.F. Cardoso, “Ultrasonic signal processing for in vivo attenuation measurement: short time fourier analysis,” *Ultrasonic Imaging*, vol. 5, no. 2, pp. 117–135, 1983.
- [13] R. Kuc, “Estimating acoustic attenuation from reflected ultrasound signals: Comparison of spectral-shift and spectral-difference approaches,” *IEEE Transactions on Acoustics, Speech, and Signal Processing*, vol. 32, no. 1, pp. 1–6, 1984.
- [14] T. Baldewek, P. Laugier, A. Herment, and G. Berger, “Application of autoregressive spectral analysis for ultrasound attenuation estimation: interest in highly attenuating medium,” *IEEE Transactions on Ultrasonics, Ferroelectrics, and Frequency Control*, vol. 42, no. 1, pp. 99–110, 1995.
- [15] Kayvan Samimi and Tomy Varghese, “Optimum diffraction-corrected frequency-shift estimator of the ultrasonic attenuation coefficient,” *IEEE Transactions on Ultrasonics, Ferroelectrics, and Frequency Control*, vol. 63, no. 5, pp. 691–702, 2016.
- [16] Hyungsuk Kim and Tomy Varghese, “Hybrid spectral domain method for attenuation slope estimation,” *Ultrasound in Medicine & Biology*, vol. 34, no. 11, pp. 1808–1819, 2008.
- [17] Lin Xin Yao, James A Zagzebski, and Ernest L. Madsen, “Backscatter coefficient measurements using a reference phantom to extract depth-dependent instrumentation factors,” *Ultrasonic Imaging*, vol. 12, no. 1, pp. 58–70, 1990.
- [18] Yassin Labyed and Timothy A. Bigelow, “A theoretical comparison of attenuation measurement techniques from backscattered ultrasound echoes,” *The Journal of the Acoustical Society of America*, vol. 129, no. 4, pp. 2316–2324, 2011.
- [19] Andres Coila, Julien Rouyer, Omar Zenteno, and Roberto Lavarello, “A regularization approach for ultrasonic attenuation imaging,” in *2016 IEEE 13th International Symposium on Biomedical Imaging (ISBI)*. IEEE, 2016, pp. 469–472.
- [20] Andres L. Coila and Roberto Lavarello, “Regularized spectral log difference technique for ultrasonic attenuation imaging,” *IEEE Transactions on Ultrasonics, Ferroelectrics, and Frequency Control*, vol. 65, no. 3, pp. 378–389, 2017.

- [21] Andres Coila, Rosa Laines, Claudia Salazar, Julien Rouyer, Gabriel Jimenez, Joseph A Pinto, Jorge Guerrero, and Roberto Lavarello, “In vivo attenuation estimation in human thyroid nodules using the regularized spectral log difference technique: Initial pilot study,” in *2017 IEEE International Ultrasonics Symposium (IUS)*. IEEE, 2017, pp. 1–4.
- [22] Ana Cecilia Saavedra, Benjamin Castaneda, and Roberto J. Lavarello, “Multi-wave dermis characterization using attenuation coefficient and shear wave speed estimates in vivo,” in *2019 IEEE International Ultrasonics Symposium (IUS)*. IEEE, 2019, pp. 1269–1272.
- [23] Farah Deeba, Ricky Hu, Jefferson Terry, Denise Pugash, Jennifer A. Hutcheon, Chantal Mayer, Septimiu Salcudean, and Robert Rohling, “A spatially weighted regularization method for attenuation coefficient estimation,” in *2019 IEEE International Ultrasonics Symposium (IUS)*. IEEE, 2019, pp. 2023–2026.
- [24] Julien Rouyer, Andrés Coila, and Roberto Lavarello, “Improving local attenuation estimation using a spatial regularization strategy over frequencies,” in *2016 IEEE International Ultrasonics Symposium (IUS)*. IEEE, 2016, pp. 1–4.
- [25] Simon R. Cherry, “Multimodality in vivo imaging systems: twice the power or double the trouble?,” *Annu. Rev. Biomed. Eng.*, vol. 8, pp. 35–62, 2006.
- [26] Simon R. Arridge, Matthias J. Ehrhardt, and Kris Thielemans, “(an overview of) synergistic reconstruction for multimodality/multichannel imaging methods,” *Philosophical Transactions of the Royal Society A*, vol. 379, no. 2200, pp. 20200205, 2021.
- [27] Laurent M. Mugnier, Jean-Marc Conan, Thierry Fusco, and Vincent Michau, “Joint maximum a posteriori estimation of object and psf for turbulence-degraded images,” in *Bayesian Inference for Inverse Problems*. International Society for Optics and Photonics, 1998, vol. 3459, pp. 50–61.
- [28] Chen Chen, Yeqing Li, and Junzhou Huang, “Calibrationless parallel mri with joint total variation regularization,” in *Medical Image Computing and Computer-Assisted Intervention–MICCAI 2013: 16th International Conference, Nagoya, Japan, September 22–26, 2013, Proceedings, Part III 16*. Springer, 2013, pp. 106–114.
- [29] Junzhou Huang, Chen Chen, and Leon Axel, “Fast multi-contrast mri reconstruction,” *Magnetic Resonance Imaging*, vol. 32, no. 10, pp. 1344–1352, 2014.
- [30] Matthias J. Ehrhardt, Kris Thielemans, Luis Pizarro, David Atkinson, Sébastien Ourselin, Brian F. Hutton, and Simon R. Arridge, “Joint reconstruction of pet-mri by exploiting structural similarity,” *Inverse Problems*, vol. 31, no. 1, pp. 015001, 2014.
- [31] Matthias J. Ehrhardt, Pawel Markiewicz, Maria Liljeroth, Anna Barnes, Ville Kolehmainen, John S Duncan, Luis Pizarro, David Atkinson, Brian F. Hutton, Sébastien Ourselin, et al., “Pet reconstruction with an anatomical mri prior using parallel level sets,” *IEEE Transactions on Medical Imaging*, vol. 35, no. 9, pp. 2189–2199, 2016.

- [32] Daniil Kazantsev, Jakob S. Jørgensen, Martin S. Andersen, William R.B. Lionheart, Peter D. Lee, and Philip J. Withers, “Joint image reconstruction method with correlative multi-channel prior for x-ray spectral computed tomography,” *Inverse Problems*, vol. 34, no. 6, pp. 064001, 2018.
- [33] M.J. Ehrhardt, *Joint reconstruction for multi-modality imaging with common structure*, Ph.D. thesis, UCL (University College London), 2015.
- [34] David S. Rigie and Patrick J. La Rivière, “Joint reconstruction of multi-channel, spectral ct data via constrained total nuclear variation minimization,” *Physics in Medicine & Biology*, vol. 60, no. 5, pp. 1741, 2015.
- [35] David S. Rigie, Adrian A. Sanchez, and Patrick J. La Rivière, “Assessment of vectorial total variation penalties on realistic dual-energy ct data,” *Physics in Medicine & Biology*, vol. 62, no. 8, pp. 3284, 2017.
- [36] Jing Tang and Arman Rahmim, “Anatomy assisted pet image reconstruction incorporating multi-resolution joint entropy,” *Physics in Medicine & Biology*, vol. 60, no. 1, pp. 31, 2014.
- [37] Angshul Majumdar and Rabab K. Ward, “Joint reconstruction of multiecho mr images using correlated sparsity,” *Magnetic Resonance Imaging*, vol. 29, no. 7, pp. 899–906, 2011.
- [38] Viswanath P. Sudarshan, Gary F. Egan, Zhaolin Chen, and Suyash P. Awate, “Joint pet-mri image reconstruction using a patch-based joint-dictionary prior,” *Medical Image Analysis*, vol. 62, pp. 101669, 2020.
- [39] Hemant Kumar Aggarwal, Merry P. Mani, and Mathews Jacob, “Model based image reconstruction using deep learned priors (modl),” in *2018 IEEE 15th International Symposium on Biomedical Imaging (ISBI 2018)*. IEEE, 2018, pp. 671–674.
- [40] Jiashuo Lyu, Chao Tan, and Feng Dong, “Image reconstruction for ultrasonic tomography using multi-channel convolutional neural network,” in *2020 39th Chinese Control Conference (CCC)*. IEEE, 2020, pp. 7304–7309.
- [41] Laurent Condat, “A primal–dual splitting method for convex optimization involving lipschitzian, proximable and linear composite terms,” *Journal of Optimization Theory and Applications*, vol. 158, no. 2, pp. 460–479, 2013.
- [42] Edmundo A. Miranda, Adrian Basarab, and Roberto Lavarello, “Total nuclear variation spectral log difference for ultrasonic attenuation images,” in *2023 IEEE 20th International Symposium on Biomedical Imaging (ISBI)*. IEEE, 2023, pp. 1–4.
- [43] Edmundo A. Miranda, Adrian Basarab, and Roberto Lavarello, “Multifrequency joint reconstruction of ultrasonic attenuation images,” in *2023 IEEE International Ultrasonics Symposium (IUS)*. IEEE, 2023, pp. 1–4.

- [44] Dinah Maria Brandner, Xiran Cai, Josquin Foiret, Katherine W Ferrara, and Bernhard G Zagar, “Estimation of tissue attenuation from ultrasonic b-mode images—spectral-log-difference and method-of-moments algorithms compared,” *Sensors*, vol. 21, no. 7, pp. 2548, 2021.
- [45] Zhaojun Wu, Qiang Wang, Jing Jin, and Yi Shen, “Structure tensor total variation-regularized weighted nuclear norm minimization for hyperspectral image mixed denoising,” *Signal Processing*, vol. 131, pp. 202–219, 2017.
- [46] Laurent Condat, “A generic proximal algorithm for convex optimization-application to total variation minimization,” *IEEE Signal Processing Letters*, vol. 21, no. 8, pp. 985–989, 2014.
- [47] B. E. Treeby, J. Jaros, A. P Rendell, and B.T. Cox, “Modeling nonlinear ultrasound propagation in heterogeneous media with power law absorption using ak-space pseudospectral method,” *The Journal of the Acoustical Society of America*, vol. 131, no. 6, pp. 4324–4336, 2012.
- [48] Paul Rodríguez and Brendt Wohlberg, “Efficient minimization method for a generalized total variation functional,” *IEEE Transactions on Image Processing*, vol. 18, no. 2, pp. 322–332, 2008.
- [49] Bastian Goldluecke, Evgeny Strelakovski, and Daniel Cremers, “The natural vectorial total variation which arises from geometric measure theory,” *SIAM Journal on Imaging Sciences*, vol. 5, no. 2, pp. 537–563, 2012.
- [50] Muhammed Yusuf Waziri and Amar Elgaili Mahmoud, “Weighted frobenius norm diagonal quasi-newton method for solving large-scale system of nonlinear equations,” in *Journal of Physics: Conference Series*. IOP Publishing, 2018, vol. 1123, p. 012050.
- [51] Shuhang Gu, Lei Zhang, Wangmeng Zuo, and Xiangchu Feng, “Weighted Nuclear Norm Minimization with Application to Image Denoising,” in *2014 IEEE Conference on Computer Vision and Pattern Recognition*, 2014, pp. 2862–2869.
- [52] Shuhang Gu, Qi Xie, Deyu Meng, Wangmeng Zuo, Xiangchu Feng, and Lei Zhang, “Weighted nuclear norm minimization and its applications to low level vision,” *International Journal of Computer Vision*, vol. 121, pp. 183–208, 2017.
- [53] Andres Coila, *Quantitative ultrasound and the effects of acoustic nonlinearity*, Ph.D. thesis, University of Illinois Urbana-Champaign, 2022.
- [54] Tim Koch, Sannachi Lakshmanan, Sebastian Brand, Michael Wicke, Kay Raum, and Daniel Mörlein, “Ultrasound velocity and attenuation of porcine soft tissues with respect to structure and composition: Ii. skin and backfat,” *Meat Science*, vol. 88, no. 1, pp. 67–74, 2011.
- [55] Kevin M. Holt, “Total nuclear variation and jacobian extensions of total variation for vector fields,” *IEEE Transactions on Image Processing*, vol. 23, no. 9, pp. 3975–3989, 2014.